Investigating the Physicochemical Properties of an Extra-large Pore Aluminosilicate ZEO-1

Mohammad Fahda, Jawad Fayek, Eddy Dib, Hugo Cruchade, Nathan Pichot, Nourrdine Chaouati, Ludovic Pinard, Petko St. Petkov, Georgi N Vayssilov, Alvaro Mayoral, et al.

Investigating the physicochemical properties of an extra-large pore aluminosilicate ZEO-1†

Mohammad Fahda[a], Jawad Fayek[b], Eddy Dib[a], Hugo Cruchade[a], Nathan Pichot[a], Nourrdine Chaouati[a], Ludovic Pinard[a], Petko St. Petkov[c], Georgi N. Vayssilov[c], Alvaro Mayoral[d], Bernhard Witulski[b], Louwanda Lakiss[a], and Valentin Valtchev*[a,c]

[a]Laboratoire Catalyse et Spectrochimie (LCS), Normandie Université, ENSICAEN, UNICAEN, CNRS, Caen, 14050 (France)

[b]Laboratoire de Chimie Moléculaire et Thio-organique (LCMT), Normandie Université, ENSICAEN, UNICAEN, CNRS, Caen, 14050 (France)

[c]University of Sofia, Faculty of Chemistry and Pharmacy, 1126 Sofia, (Bulgaria)

[d]Instituto de Nanociencia y Materiales de Aragón (INMA), CSIC-Universidad de Zaragoza,Zaragoza, 50009 (Spain)

*Email: Valentin.Valtchev@ensicaen.fr

†Supporting Information available.

Abstract

ZEO-1 is the first stable extra-large pore zeolite with a substantial amount of aluminum in the framework achieved directly upon synthesis, and here we present a comprehensive analysis of its physicochemical properties. Our findings show that varying the different synthesis parameters of ZEO-1 allows for controlling its crystallization kinetics, crystal size, and morphology. Investigating the acidic properties of ZEO-1 using ^{27}Al and ^{1}H solid-state nuclear magnetic resonance shows that ZEO-1 exhibits potentially three different aluminum populations. The acidic nature of the hydroxyl species within ZEO-1 is studied using pyridine and 2,6-ditert-butylpyridine and carbon monoxide via *in situ* infrared spectroscopy, where the extinction coefficient for the 1545 cm^{-1} pyridinium band is determined. Density functional theory modeling suggests that the active sites within ZEO-1 potentially occupy four different tetrahedral sites, where three of these sites are most likely located within the 12-membered ring channel, while one site is located in the 16-membered ring channel. The catalytic performance comparison of ZEO-1 with zeolites Beta and USY in the alkylation of phenol by tert-butyl alcohol, *n*-hexane cracking, and anisole dismutation reveals intriguing insights. ZEO-1 exhibits selectivity similar to Beta zeolite, consistent with density functional theory modeling predictions. Despite displaying weaker overall Brønsted acid sites compared to Beta, ZEO-1's acidity remains comparable to USY zeolite. Moreover, ZEO-1 demonstrates consistent performance relative to large pore zeolites with enhanced stability in the anisole dismutation test.

TOC graphic

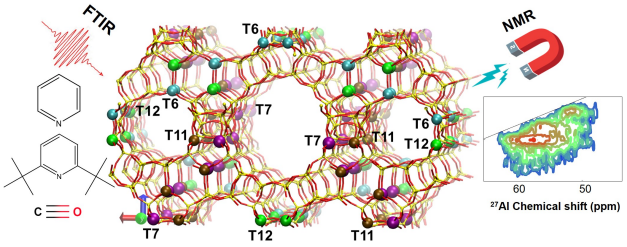

For the first time in zeolite history, the acidic properties of a stable extra-large pore aluminosilicate are reported.

1 Introduction

Zeolites are a unique family of inorganic, highly crystalline materials with exceptional hydrothermal stability even at high temperatures. Their microporosity introduces a molecular sieving effect, improving selectivity for various reactions, including cracking and isomerization. Furthermore, unlike amorphous aluminosilicates, the Brønsted acid sites in zeolites can be tuned through synthesis or partial ion exchange, enabling precise characterization in terms of location and strength. This tunability allows for more controlled catalytic performance[1,2].

However, by the 1980s, zeolites had a maximum pore opening of 0.74 nm, represented by the well-known 12-membered ring Faujasite structure, which serves as a powerful catalyst for hydrocarbon upgrading[3,4]. This limited pore opening restricts the upgrading of heavy hydrocarbon fractions. Consequently, there is a demand for extra-large pore zeolites to expand the operational limits and overcome the mass transfer limitations imposed by the narrow micropores, which can lead to faster catalyst deactivation[5–8]. In 1995, the discovery of the first pure silicate extra-large pore material, UTD-1 (**DON**), was reported[9,10]. Since then, the number of extra-large pore zeolites reported and registered in the International Zeolite Association Database (IZA) has reached 27[11]. These zeolites have been synthesized as pure silicates, aluminosilicates, borosilicates, germanosilicates, and aluminophosphates. Several dedicated reviews in the literature discuss the details of these zeolite types[12–14].

Despite the feasibility of synthesizing extra-large pore zeolites, no industrial endorsement exists for these materials. This lack of industrial adoption mainly stems from the stability of the materials and the nature of active sites incorporated within their frameworks. For instance, germanosilicate extra-large pore zeolites would undergo significant amorphization under ambient humid conditions during calcination and the removal of the structure directing agent (SDA) due to the liability of germanium bonds to hydrolysis by water molecules[15,16]. As for pure silicate, aluminosilicate, and borosilicate extra-large pore zeolites, while they do exhibit robust chemical and thermal stability upon calcination and removal of the SDA, incorporating aluminum within the framework has been particularly challenging. Despite the employment of different protocols, such as synthesis by seeding and post-synthetic alumination, the aluminum

loading has never been satisfactory for catalytic applications (a maximum of Si/Al = 35)[9,17–19].

Recently, a noteworthy discovery in the field of zeolite synthesis is the extra-large pore aluminosilicate zeolite, ZEO-1 (**JZO**), which exhibits a relatively lower Si/Al ratio of 15 achievable directly during synthesis using a phosphonium-based SDA (see Figure S1)[20]. ZEO-1 boasts a three-dimensional framework featuring three super cages formed by interconnected 16+16, 16+12, and 16+12 channels. It demonstrates robust hydrothermal stability during calcination and SDA removal under atmospheric conditions. Additionally, the 16-ring pore apertures remain free from any geometrical distortions caused by interrupted silicon species (such as the case with -**EWT**[21] and -**SSO**[22]) that could otherwise reduce the effective diameter of the ring, thereby altering its behavior to resemble that of large or medium pore zeolites. The synthesis of ZEO-1 marks a significant breakthrough in zeolite synthesis, showcasing unprecedented properties that position it as a highly promising catalyst for future applications.

In this work, we study the effect of the different parameters involved in the synthesis of ZEO-1, including the aluminum source, the fluoride content, the initial Si/Al ratio, the water content, and the synthesis temperature on the total duration to obtain this material and its impact on the physical properties of ZEO-1. Then, we investigate the accessibility and strength of the acid sites in ZEO-1 by combining solid-state nuclear magnetic resonance (NMR) and in situ infrared spectroscopy where pyridine (Py), 2,6-ditert-butylpyridine (DTBPY), and carbon monoxide are used as basic probe molecules. The relative stability of Al location in different tetrahedral atom (T-atom) positions in the framework and the acidity of the corresponding bridging hydroxyls was estimated by periodic density functional calculations. Finally, the catalytic performance of ZEO-1 in the phenol alkylation by tert-butyl alcohol, *n*-hexane cracking, and anisole disproportionation is evaluated and compared to large pore zeolite types (Beta (***BEA**) and USY (**FAU**).

2 Experimental section

2.1 Materials

All the chemicals listed herein have been used as received from the supplier without further purification:

Tricyclohexylphosphine (BLD Pharmatech Ltd., 97%), Methyl iodide (Sigma-Aldrich, 99.5%), Acetonitrile (Fisher Scientific, 98%), Ambersep 900 hydroxide resin (Thermo Fisher Scientific), Ludox HS-40 (Sigma-Aldrich), (Aluminum isopropoxide (Fluka, 98%), Sodium Aluminate (Sigma-Aldrich, 44% Na_2O, 56% Al_2O_3), Cesium nitrate (Sigma-Aldrich, 98%), Hydrofluoric acid 40 wt% (Fisher Scientific, 98%), Ammonium chloride (Fisher Scientific, 98%), Zeolite Beta (Zeolyst, CP814E*), Zeolite USY CBV-712 (Zeolyst).

2.2 Synthesis of Methyltricyclohexylphosphonium SDA

In an argon-purged Schlenk tube, tricyclohexylphosphine (10 g, 35.6 mmol, 1 equiv.) was dissolved in acetonitrile (40 ml). Subsequently, methyl iodide (19.58g, 138 mmol, 3.87 equiv.) was added dropwise to the solution. The reaction proceeded at room temperature within 48 hours. The solvent and excess methyl iodide were then removed under reduced pressure, resulting in the formation of the final product tricyclohexylmethylphosphonium iodide, which has been analyzed using liquid proton, carbon, and phosphorus NMR to confirm its purity (15g, 35.5 mmol, 98%).

^{1}H NMR (500 MHz, $CDCl_3$) δ 2.62 (qt, J = 12.1 Hz, J = 2.9 Hz, 3H), 2.02 (m, 9H), 1.94 (m, 6H), 1.80 (m, 3H), 1.50 (m, 12H), 1.32 (qt, J = 12.9, J = 3.4 Hz, 3H).

^{13}C NMR (125 MHz, $CDCl_3$) δ 30.2 (CH, d, $^1J_{(c\text{-}p)}$ = 42.2 Hz), 26.9 (CH_2, d, $^3J_{(c\text{-}p)}$ = 3.8 Hz), 26.3 (CH_2, d, $^2J_{(c\text{-}p)}$ = 12.2 Hz), 25.3 (CH_2, d, $^4J_{(c\text{-}p)}$ = 1.4 Hz), 0.1 (CH_3, d, $^1J_{(c\text{-}p)}$ = 49.1 Hz).

^{31}P NMR (202 MHz, $CDCl_3$) δ 33.9 ppm

Melting point: 186.7 - 187.9 2.5 ^{o}C/min

Tricyclohexylmethylphosphonium iodide has been converted into hydroxide by using Ambersep 900 hydroxide resin. In a 500 ml polypropylene bottle, 10 grams of tricyclohexylmethylphosphonium iodide are added to 250 ml Milli-Q water, followed by 45 g dry resin. The SDA is left to exchange overnight. Then, the SDAOH solution is collected by filtration and concentrated to the target volume using a rotary evaporator at 60 °C. The concentrated solution is titrated by potassium hydrogen phthalate using Phenolphthalein as an indicator to determine the degree of exchange and the hydroxide concentration. The obtained basic solution has an exchange ratio of 98 % and contains 15 wt% SDAOH.

2.3 Zeolite synthesis

A general protocol for zeolite synthesis is outlined for ZEO-1 of a specific condition that applies to all the screening experiments reported in this article. In a 10 ml polypropylene bottle, 5.45 g of the SDAOH solution is added, followed by 0.068 g of Al-isopropoxide. The solution is left to stir for two hours to hydrolyze the aluminum isopropoxide properly. Then, 1.25 g of LUDOX-HS-40 is added dropwise under vigorous stirring, and the solution is left for another 1 hour to homogenize. Finally, 18.4 μL of 40 wt% hydrofluoric acid (HF) is carefully added under a well-ventilated hood to the gel mixture under vigorous stirring, after which the synthesis gel is left for aging overnight. The excess water in the synthesis gel was removed by a freeze dryer, where the weight of the bottle containing the gel was monitored every two hours until the desired water content was reached. Finally, the resulting condensed gel has the following chemical composition:

$$1SiO_2 : 0.33SDAOH : 0.05HF : 0.02Al_2O_3 : 7H_2O$$

is transferred to a 15 ml Teflon-lined stainless steel autoclave and placed in a convection heated oven at 190 °C.

The zeolite crystals are recovered by centrifugation at 21000 rpm for 10 minutes and washed with 40 ml of Milli-Q water three times to remove unreacted species and neutralize the pH.

2.4 Post-synthetic modification of as-synthesized ZEO-1

2.4.1 Calcination

The as-synthesized ZEO-1 undergoes calcination using a static oven equipped with a thermocouple, programmed as follows: a linear increase starting from room temperature, reaching 150 °C at a rate of 2.5 K/min, and maintained at 150 °C for 60 minutes to ensure mild dehydration of the zeolite. Subsequently, a linear increase from 150 °C to 600 °C at a rate of 1.9 K/min is applied, followed by a plateau at 600 °C for 6 hours to ensure the complete removal of the organic structure-directing agent (SDA) from the zeolite pores.

In instances where the main text mentions that calcined ZEO-1 is washed exclusively with water, it implies that the calcined samples were washed with 40 ml of Milli-Q water and collected by centrifugation at 21,000 rpm over three cycles, followed by drying overnight at 60 °C.

2.4.2 Ion-exchange

For the conversion of calcined ZEO-1 into its ammonium form, the following methodology is employed: 1 g of calcined ZEO-1 is suspended in 20 ml of a 0.5 M solution of ammonium chloride and placed on an oil bath at a temperature of 60 °C, rotating at 450 rpm. This process is repeated three times to ensure complete proton exchange with ammonium. Finally, the powder is recovered by centrifugation at 21,000 rpm for 10 minutes and washed with 40 ml of Milli-Q water over three cycles to remove excess ammonium chloride, followed by drying overnight at 60 °C.

The same protocol mentioned above is used to obtain the cesium form of ZEO-1, but cesium nitrate is employed as the cesium source.

2.5 Catalytic tests

2.5.1 Alkylation of phenol with tert-butyl alcohol

For the alkylation reaction of phenol with tert-butyl alcohol catalyzed by zeolite, 200 mg of the zeolite catalyst, 565 mg (0.006 mol) of phenol, and 445 mg (0.006 mol) of tert-butanol were weighed accurately. These materials were combined in a 50 ml round bottom flask. Additionally, 769 mg (0.006 mol) of nonane was added as an internal standard for chromatographic analysis.

The reaction mixture was then placed in a temperature-controlled heating mantle and maintained at 80 °C with stirring at 500 rpm for a duration of 4 hours to promote the alkylation reaction. After completion of the reaction time, the mixture was allowed to cool to room temperature. Subsequently, centrifugation at 10,000 rpm for 4 minutes was performed to separate the solid catalyst from the reaction mixture. The supernatant obtained after centrifugation was carefully retrieved, excluding any solid residue from the catalyst. The distribution of the products was determined by analyzing the supernatant on a SCION gas chromatograph equipped with a 5MS column (30 m length, 0.25 mm diameter, and 0.2 μm thickness).

2.5.2 *n*-Hexane cracking

The catalytic test of the *n*-hexane cracking was performed in a four-parallel fixed-bed reactor unit. Different masses of the same catalyst with a particle size of 0.2-0.5 mm were put in each reactor (20, 40, 60, and 80 mg) and pre-treated at 813 K under nitrogen flow for 12 h. *n*-Hexane (99.99 % pure from Sigma Aldrich) was then diluted in nitrogen flow and injected in the reactors at 813 K with a molar ratio of 11 ($P_{N_2}/P_{C_6H_{14}}$). The activity of each zeolite is measured by estimating the conversion by varying the weight hour space velocity (WHSV). Reaction products were analyzed online in GC450 gas Chromatography equipped with a C_p-Al_2O_3/Na_2SO_4 capillary column (50 m, 10 μm) coupled with an FID detector. The Turn Over Frequency (TOF, h^{-1}) was calculated as follows:

$$\text{TOF} = \frac{A}{[H^+] \times M_{n-\text{hexane}}}$$

A ($g/h/g_{catalyst}$) is the catalyst activity estimated graphically by the initial slope of the plot -Ln(1-X) Vs 1/WHSV. X is the conversion, and WHSV is the weight hour space velocity in $g_{n\text{-hexane}}\ g^{-1}\ h^{-1}$. $[H^+]$ is the concentration of Brønsted acid sites of the catalyst determined by pyridine ($mol/g_{catalyst}$), and $M_{n\text{-hexane}}$ is the molar weight of the *n*-hexane (g/mol)

2.5.3 Anisole disproportionation

The dismutation of anisole (9.95 mg/min) was carried out under N_2 flow (100 mL/min) in a fixed bed glass reactor (75 cm, internal $\varnothing$= 0.45 cm). Prior to the reaction, catalysts are compacted (< 0.5 tonne), crushed, and sieved to 0.2 < $\varnothing$< 0.4 mm homogeneous particles. Catalyst mass was varied (between 10 and 40 mg) in order to vary the contact time between feed and active sites. Catalysts were dried under constant N_2 flow (100 mL/min) at 120 °C (heating ramp 1 °C/min) for one hour, then heated up to 400 °C (4 °C/min) for one hour prior to anisole injection. Reaction products are samples and stored in sample loops during the 1 h reaction, then injected into GC-FID (Column SC-5MS, 30 m – 0.25 mm – 25 μm).

Anisole conversion (X, wt.%) and product yields (Y, wt.%) are calculated using the following equations:

$$X(\text{ wt. \%}) = \left(1 - \frac{A_{\text{Anisole}}}{A_{\text{tot}}}\right) * 100$$

$$Y_{\text{prod}}\ (\text{ wt. \% }) = \left(\frac{A_{\text{prod}}}{A_{\text{tot}}}\right) * 100$$

Where $A_{Anisole}$ is the peak area of anisole (GC-FID), A_{tot} is the sum of all peak areas in the chromatogram, and A_{prod} is the peak area of the targeted product.

The catalyst activity α_i is determined using the following formula:

$$-\ln(1 - X_i) = \alpha_i * \frac{W_{\text{cata}}}{F_{\text{feed}}}$$

Where W_{cata} is the catalyst mass and F_{feed} corresponds to the mass flow of anisole.

The modeling of the catalysts' activity against time on stream (TOS) is shown in Figure 11

of the main text, and follows, for all zeolites, an inverse exponential law of deactivation, as shown by the following equation:

$$\alpha_i = \alpha_1 e^{-k_D * TOS} + \alpha_2 \tag{1}$$

With α_i being the activity at any i TOS, α_1 represents the activity originating from the acid sites that will cease to participate in the conversion process, and $\alpha_1 + \alpha_2 = \alpha_0$, the initial activity. α_2 is the residual activity at the steady state.

3 Results and Discussion

3.1 Synthesis of ZEO-1

3.1.1 Influence of synthesis parameters on the synthesis period

Our initial interest was reproducing ZEO-1 to investigate its acidic properties and catalytic performance. However, considering the remarkable properties reported for ZEO-1, we conducted a study to explore the influence of different parameters (fluoride content, structure directing agent hydroxide (SDAOH) content, aluminum source and content, water content, and temperature) on the synthesis kinetics of ZEO-1 synthesis. An example illustrating the general synthesis protocol of the zeolites and the phosphonium SDAOH protocol is described in the experimental section. It is worth mentioning that our definition of a crystalline sample for a successful synthesis trial of ZEO-1 is the clear distinction of the two characteristic reflection peaks of ZEO-1 at 2θ = 4 and 7° and the absence of a broad peak between 2θ = 16-25° which is a characteristic of amorphous content within zeolites (see Figure S2). Finally, each synthesis experiment presented in this manuscript has been repeated twice to ensure the accuracy of the synthesis period. The different synthesis parameters are summarized in Table 1 using aluminum isopropoxide (Al(O-i-Pr)$_3$) and sodium aluminate ($Na_2O.Al_2O_3$) as aluminum precursors.

Using Al(O-i-Pr)$_3$ and for a fixed Si/SDAOH ratio of 3, the shortest period of time to obtain ZEO-1 is achieved at Si/F = 20, corresponding to 16 days. Upon increasing the fluoride content by a factor of two (Si/F = 10), the synthesis duration doubles to reach 29 days, while reducing the fluoride content (Si/F = 30) results in an amorphous phase. This suggests that fluoride at this ratio plays a structure-stabilizing role by accelerating the formation kinetics of ZEO-1 rather than acting as a mineralizing agent. For a fixed Si/F ratio of 20 and varying Si/SDAOH from 2 to 4, it becomes evident that the SDAOH concentration does not significantly influence the kinetics of ZEO-1 synthesis, as the crystallization time remained similar.

Table 1: Time in days needed to synthesize ZEO-1 using aluminum isopropoxide ($Al(O\text{-}i\text{-}Pr)_3$) or sodium aluminate ($Na_2O.Al_2O_3$) as aluminum precursors, and Ludox HS-40 as the silica source along with the resulting Si/Al ratio after synthesis for the as-synthesized samples

.

		Time (days)	Si/Al[a]
Aluminum isopropoxide as an aluminum source			
Si/Al = 25 | Si/SDAOH = 3 | H_2O/Si = 7 | 190 °C			
Si/F	10	29	20.1
	20	16	19.5
	30	30[†]	-
Si/Al = 25 | Si/F = 20 | H_2O/Si = 7 | 190 °C			
Si/SDAOH	2	16	21.7
	3	16	19.5
	4	16	22.4
Si/Al = 25 | Si/F = 20 | Si/SDAOH = 3 | 190 °C			
H_2O/Si	7	16	19.5
	15	31	20.0
Si/F = 20 | Si/SDAOH = 3 | H_2O/Si = 7 | 190 °C			
Si/Al	15	31*	13.4
	20	23	16.7
	25	16	19.5
Sodium aluminate as an aluminum source			
Si/Al = 25 | Si/Na = 19.3 | Si/SDAOH = 3 | H_2O/Si = 7 | 190 °C			
Si/F	∞	12*	21.2
	20	8*	20.1
Si/Al = 25 | Si/Na = 19.3 | Si/F = 20 | Si/SDAOH = 3 | 190 °C			
H_2O/Si	7	8*	20.1
	15	21	20.9
Si/Na = 19.3 | Si/F = 20 | Si/SDAOH = 3 | H_2O/Si = 7 | 190 °C			
Si/Al[b]	15	8*	13.2
	25	8*	20.1
	50	8	46.3
Si/Al = 25 | Si/Na = 19.3 | Si/F = 20 | Si/SDAOH = 3 | H_2O/Si = 7			
Temperature (°C)	150	40	20.7
	170	21	21.5
	190	8*	20.1

[†] Amorphous material is obtained after 35 days of hydrothermal treatment.
[*] Mordenite is obtained as an impurity.
[a] Determined by inductive coupling plasma analysis (ICP).
[b] For the experiments with Si/Al ratios of 15, 25, and 20, the Si/Na ratios were 11.6, 19.3, and 38.7, respectively.

The presence of alkali cations is known to accelerate the kinetics of zeolite synthesis[23]. Therefore, we used sodium aluminate as an aluminum source, which contains around 44 wt% of sodium oxide. Table 1 demonstrates that using sodium aluminate instead of aluminum isopropoxide increases the crystallization kinetics by a factor of 2, where crystalline ZEO-1 is obtained within 8 days instead of 16 days. Figure 1 shows that under the same conditions (Si/Al = 25 | Si/SDAOH = 3 | Si/F = 20 | H_2O/Si = 7 | 190 °C), using aluminum isopropoxide yields pure ZEO-1, as evidenced by the observed PXRD pattern closely matching the simulated pattern of ZEO-1. However, when using sodium aluminate mordenite (**MOR**), marked by an asterisk in Figure 1 is obtained as a competing phase. Moreover, ZEO-1 can be synthesized in fluoride-free conditions in only 12 days when sodium aluminate is used, requiring only four extra days, which suggests a less pronounced impact of fluoride ions on the synthesis kinetics compared to when aluminum isopropoxide is used.

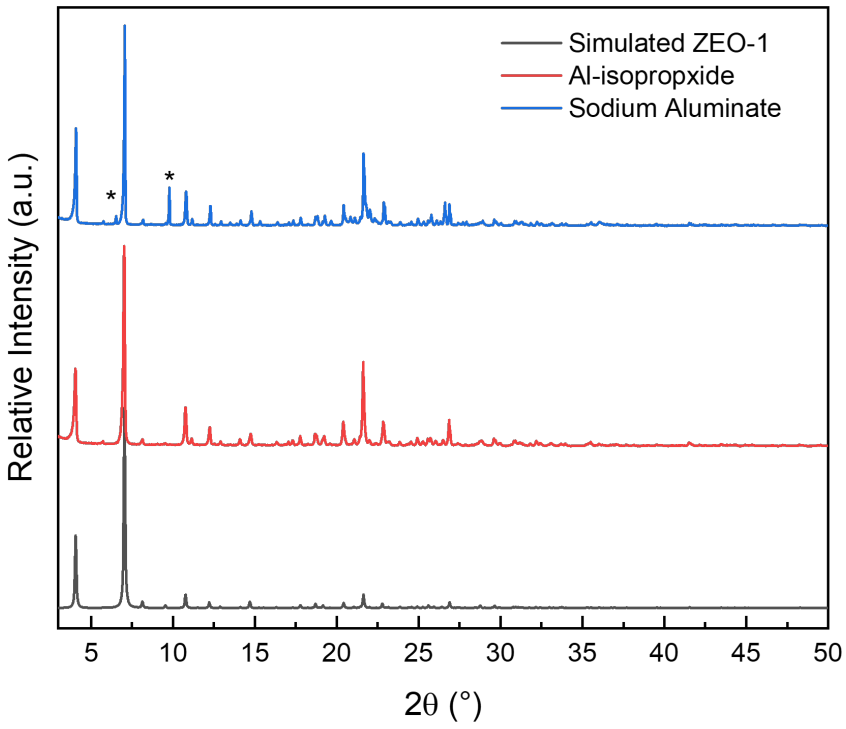

Figure 1: PXRD patterns for as-synthesized ZEO-1 under the same conditions (Si/Al = 25 | Si/SDAOH = 3 | Si/F = 20 | H_2O/Si = 7 | 190 °C) using two different aluminum sources compared to the simulated pattern of ZEO-1. *Mordenite impurity.

The water content (H_2O/Si) influences only the kinetic aspects rather than any phase selectivity, as ZEO-1 was obtained for both synthesis systems. When the H_2O/Si ratio is doubled from 7 to 15, the synthesis time doubles for the aluminum isopropoxide system and nearly triples for the system employing sodium aluminate. Nonetheless, the latter remains faster. This shows that while a supersaturated gel promotes faster crystallization kinetics, it is not necessarily a prerequisite. Even relatively dilute gels have been found to effectively direct the formation of ZEO-1, highlighting the robust nature of this material's "SDA-Framework" interaction.

The influence of the temperature's effect was studied only for the sodium aluminate system, as it exhibits significantly shorter synthesis times, making observations more feasible. Table 1 reveals that ZEO-1 can be synthesized at three different temperatures: 190, 170, and 150 °C, with lower temperatures requiring a pronounced longer time for zeolite crystallization. Furthermore, when ZEO-1 is synthesized at 170 and 150 °C, mordenite is not detected as a competing phase, probably due to the lower reaction temperature relative to 190 °C, which might hinder the formation of mordenite as an impurity.

As for the gel composition's initial Si/Al ratio, it is possible to decrease it down to 15 for both systems, resulting in a fixed synthesis duration of 8 days when sodium aluminate is employed compared to 31 days for Al(O-i-Pr)$_3$. Nevertheless, mordenite is obtained as a competing phase in both cases. Interestingly, by using sodium aluminate, it is possible to synthesize pure ZEO-1 similarly in 8 days starting from a higher Si/Al ratio of 50, which suggests that mordenite is formed at 190 °C by the unreacted aluminum and sodium species accelerated by the high temperature.

In examining the impact of synthesis conditions on the resulting Si/Al ratio for the as-synthesized ZEO-1 shown in Table 1, it is evident that only the initial Si/Al ratio of the precursor gel significantly influences the aluminum content, while the other parameters result in Si/Al ratios close to 20. When either aluminum source is used to attain a Si/Al ratio of 15 in the mother gel, the final aluminum content of ZEO-1 approaches a threshold of 13. Conversely, utilizing sodium aluminate with an initial Si/Al ratio of 50 leads to a notable decrease in the

final aluminum loading within ZEO-1, with a Si/Al ratio reaching up to 46.

3.1.2 Effect of the synthesis parameters on the size and morphology of ZEO-1 crystals

The different synthesis parameters and choice of aluminum source appear to influence the size and morphology of ZEO-1 crystals dramatically, and the results are summarized in Table 2.

The strongest influence, in terms of size and morphology, comes from the choice of the aluminum source. The SEM images for ZEO-1 synthesized under the same conditions (Si/Al = 25 | Si/SDAOH = 3| Si/F = 20, H_2O/Si = 7 | 190 °C) are shown in Figure 2. When aluminum isopropoxide is employed as the aluminum source, these crystals exhibit an ill-defined spherical shape, and their particle size measures 110 ± 19 nm. However, when sodium aluminate is used, the crystal size undergoes a substantial increase of nearly 16-fold, resulting in crystals with an average size of 1.73 ± 0.28 μm. Additionally, these crystals exhibit a leaf-like and isometric morphology.

The fluoride and aluminum content is observed to influence only the crystal size without impacting the morphology of ZEO-1 crystals where the ill-defined spheres morphology is retained. When Al(O-i-Pr)$_3$ was used, doubling the fluoride content from Si/F = 20 to 10 resulted in a slight increase in crystal size, growing from around 110 ± 19 nm to 170 ± 30 nm. On the other hand, in the case of the sodium aluminate system, the presence of fluoride during synthesis led to a minor reduction in crystal size, decreasing from 1.9 ± 0.37 μm to 1.7 ± 0.28 μm when compared to the fluoride-free synthesis (see Figure S3).

Furthermore, increasing the aluminum content for both systems tends to favor the formation of smaller zeolite crystals. When using Al(O-i-Pr)$_3$, the crystal size decreases from 110 to 71 nm upon decreasing the Si/Al ratio from 25 to 15. Similarly, when using sodium aluminate, the crystal size decreases from 2.3 ± 0.3 μm to 1.5 ± 0.29 μm upon decreasing the Si/Al ratio from 50 to 15 (refer to SEM images in Figure S4).

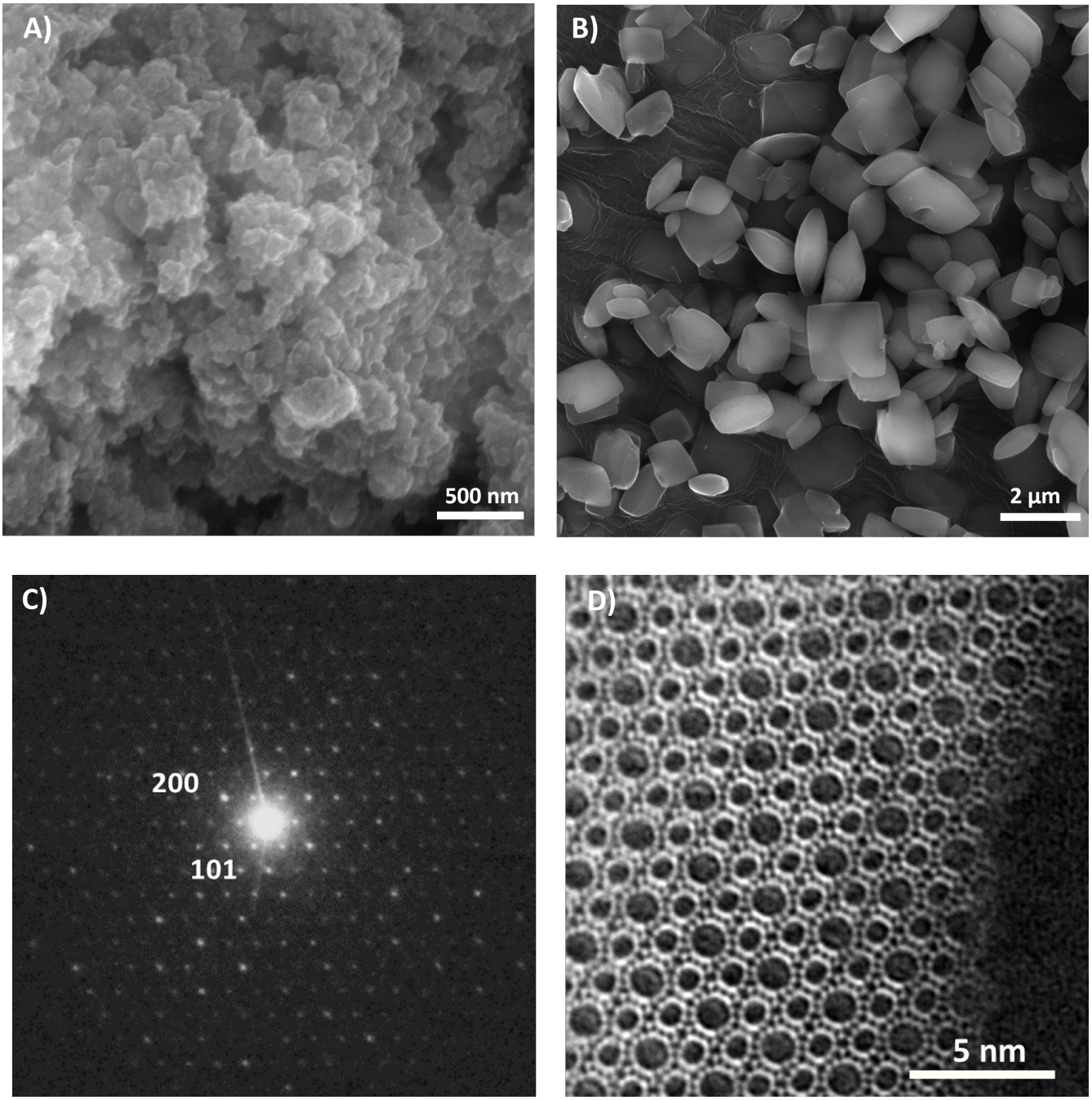

Figure 2: SEM images for as-synthesized ZEO-1 under the same conditions (Si/Al = 25 | Si/SDAOH = 3| Si/F = 20, H_2O/Si = 7 | 190 °C) using A) aluminum isopropoxide and B) sodium aluminate as sources of aluminum, C) electron microscopy analysis of the sample obtained using aluminum isopropoxide showing the electron diffraction pattern along the [100] zone axis, and D) the correspondent atomic-resolution annular dark field image showing the alternating 16- and 12-membered ring channels within ZEO-1.

Table 2: The effect of the synthesis conditions on the size and morphology of the as-synthesized ZEO-1 crystals

		Crystal Size (nm)	Morphology
Aluminum isopropoxide as an aluminum source			
Si/Al = 25 | Si/SDAOH = 3 | H_2O/Si = 7 |190 °C			
Si/F	10	170 ± 30	Ill-defined spheres
	20	110 ± 19	
Si/F = 20 | Si/SDAOH = 3 | H_2O/Si = 7 |190 °C			
Si/Al	25	110 ± 19	Ill-defined spheres
	15	71 ± 21	
Si/Al = 25 | Si/F = 20 | H_2O/Si = 7 |190 °C			
Si/SDAOH	2	1090 ± 250	Leaf-like & isometric crystals
	3	110 ± 19	Ill-defined spheres
	4	93 ± 25	Spherical aggregation of crystals
Si/Al = 25 | Si/F = 20 | Si/SDAOH= 3 |190 °C			
H_2O/Si	7	110 ± 19	Ill-defined spheres
	15	863 ± 219	Leaf-like & isometric crystals
Sodium aluminate as an aluminum source			
		Crystal Size (μm)	**Morphology**
Si/Al = 25 | Si/SDAOH = 3 | H_2O/Si = 7 |190 °C			
Si/F	0	1.9 ± 0.37	Leaf-like & isometric crystals
	20	1.73 ± 0.28	
Si/F = 20 | Si/SDAOH = 3 | H_2O/Si = 7 |190 °C			
Si/Al	50	2.3 ± 0.3	Leaf-like & isometric crystals
	15	1.5 ± 0.29	
Si/Al = 25 | Si/F = 20 | Si/SDAOH = 3 | H_2O/Si = 7			
Temeprature	170 °C	-	Spherical aggregation of crystals
	150 °C	-	

The synthesis of ZEO-1 in a concentrated medium with low water content, characterized by H_2O/Si = 7, promotes the formation of nanosized crystals approximately 100 nm in size. Conversely, synthesis in a diluted system, reduced by a factor of 2 with an H_2O/Si = 15, favors the formation of nearly one micron-sized crystals, eight times larger than those in the concentrated system (see Figure S5). Consistent with the trends observed in previous parameters, smaller crystals around 100 nm exhibit the ill-defined sphere morphology. In comparison, larger micron-sized crystals exhibit a leaf-like morphology and isometric shape.

The amount of SDAOH significantly affects the crystal size and morphology of ZEO-1. A notable reduction in the crystal size, from approximately 1.1 μm to around 100 nm, was observed when the amount of SDAOH in the initial gel mixture was decreased from Si/SDAOH = 2 to 4. Regarding morphology, Figure S6 illustrates the distinct leaf-like and isometric crystals on the one hand and the ill-defined spheres on the other for the ZEO-1 samples synthesized with a Si/SDAOH of 2 and 3, respectively. Interestingly, another morphology was observed, characterized by spherical balls formed by aggregating ill-defined spheres at Si/SDAOH = 4.

Synthesizing ZEO-1 at temperatures lower than 190 °C appears to favor the formation of crystals in an aggregated sphere morphology, as shown in Figure S7. The crystal size was not listed in Table 2 due to the inherent challenges in estimating the crystal size in this case. However, it is evident that the agglomerates forming the spheres at 170 °C are larger and exhibit an isometric shape compared to the much smaller, ill-defined crystals forming the spheres at the synthesis temperature of 150 °C.

Concerning the spherical aggregation of crystal morphology, it might be possibly related to the rate of the polymerization/depolymerization of the ZEO-1 framework by the hydroxide ions, where decreasing the number of hydroxide ions derived from the SDAOH or operating at temperatures below 190 °C would lead to slower kinetics for ZEO-1 crystallization.

3.1.3 Scaling up ZEO-1

The screening experiments to optimize ZEO-1 synthesis were investigated at a relative microscale, where the total mass of SiO_2 in the synthesis gel was 0.5 grams. To explore the feasi-

bility of relatively scaling up ZEO-1 synthesis, the regular procedure was multiplied by a factor of 6.4, resulting in a total mass of SiO_2 of 3.2 grams in the initial synthesis gel. The chemical composition for the upscaled synthesis was: Si/Al = 25 | Si/SDAOH = 3 | Si/F = 20 | H_2O/Si = 7. The synthesis was performed at 190 °C, using Al-isopropoxide as the Aluminum source to avoid the formation of any competing phases. The synthesis was completed after 21 days, with an extra 5 days compared to the microscale experiment. Figure S8 displays the PXRD patterns of the as-synthesized scaled-up ZEO-1 after calcination at 600 °C for 6 hours, compared to the simulated pattern of ZEO-1. Both patterns match perfectly with the simulated pattern, indicating no competing phases or amorphization upon calcination, thereby confirming the superior chemical and thermal stability of ZEO-1. The inductively coupled plasma (ICP) confirms that the as-synthesized scaled-up ZEO-1 has a Si/Al ratio of around 22. The SEM images in Figure S9 illustrate that upscaling the synthesis of ZEO-1 leads to larger particles with a size of 470 ± 100 nm with an isometric shape. This particle size is notably larger than that obtained under the same conditions during the screening experiment (110 nm). However, it still remains significantly smaller than the 1.1 μm particle size achieved when sodium aluminate was employed as the aluminum source.

The textural properties of the upscaled calcined and then exchanged with NH_4Cl ZEO-1 (to remove any residual phosphorus species, which will be discussed in detail in the following section) were analyzed using nitrogen adsorption/desorption analysis. Figure S10 illustrates that ZEO-1 exhibits a type-I isotherm, a key property of ultra-microporous materials. The surface area for ZEO-1, calculated by the Roquerol-BET method, is 973 m^2/g, and the micropore volume, calculated using the t-plot equation, is 0.31 cm^3/g. Additionally, the high-resolution scanning transmission electron microscopy (HRSTEM) showcased in Figure 2C and D offers a compelling visual exploration of the pore system utilizing the annular dark field detector. These images affirm that the ZEO-1 framework exhibits a consistent pattern of alternating 16- and 12-membered ring channels, devoid of geometric distortions. This visual confirmation reinforces the paramount significance of ZEO-1 within the realm of extra-large pore zeolites.

3.2 Solid-state NMR

ZEO-1 samples investigated by solid-state NMR were synthesized under the following conditions: Si/Al = 25 | Si/SDAOH = 3 | Si/F = 20 | H_2O/Si = 7 at 190 °C using aluminum isopropoxide as an aluminum precursor. The as-synthesized ZEO-1 samples were then calcined at 600 °C then washed with either H_2O or NH_4Cl. Analysis by N_2 adsorption revealed a t-plot micropore volume of 0.29 cm^3/g for the H_2O-washed sample and 0.31 cm^3/g for the NH_4Cl-washed sample.

3.2.1 ^{29}Si NMR

Figure S11 displays the experimental and deconvoluted ^{29}Si NMR spectra for both the as-synthesized and calcined, then washed with H_2O ZEO-1 samples. The studied sample exhibits a Si/Al ratio of around 22, as determined by ICP analysis, classifying it as a high-silica zeolite. For the as-synthesized ZEO-1, six distinct resonance lines are observed at chemical shifts of -98, -101, -105, -106, -110, -116, and -119 ppm.

Resonance lines starting from -110 ppm can be unequivocally attributed to Q4(0Al) Si species, characterized by Si atoms exclusively in their local coordination sphere[24–26]. Given ZEO-1's status as a high-silica zeolite, the presence of paired aluminum species is unlikely, eliminating the possibility of silicon species with two aluminum atoms in their local coordination sphere. Therefore, assuming that the resonance lines between -95 and -100 ppm correspond solely to Q3 silanol species Si(3Si, 1OH) is reasonable.

However, assigning the resonance lines within the range of -100 ppm to -110 ppm in high-silica zeolites is a challenging task due to the overlapping signals from silanol species and the signal corresponding to the presence of one aluminum atom in the local coordination sphere of Q4 silicon species Si(3Si, 1Al). Upon calcination, the ^{29}Si NMR spectrum undergoes significant changes, with a marked reduction in the intensity of the resonance lines at -105 and -106 ppm. This can possibly be due to the expulsion of tetrahedral framework aluminum to form octahedral extra-framework aluminum, as will be discussed in the 27Al NMR analysis part. Similarly, the resonance lines at -116 and -119 ppm become barely discernible, suggesting a

slight angular distortion of the ZEO-1 framework upon the SDA removal (see Figure S12 for a direct comparison).

3.2.2 ^{27}Al NMR

The ^{27}Al NMR spectrum for the as-synthesized ZEO-1, presented in Figure 3, reveals a single prominent resonance line at approximately 56 ppm and an overlapping band at 54 ppm. These signals correspond to aluminum species with tetrahedral coordination. Upon calcination, the spectral line at 56 ppm remains unchanged; however, the appearance of a sharp peak at 0 ppm and a broad band ranging from 0 to -9 ppm can be attributed to the formation of monomeric and polymeric extra-framework aluminum (EFAL) species, respectively[27,28]. This indicates that the aluminum species within ZEO-1 remains exceptionally stable.

As will be discussed in the infrared spectroscopy section, it is more convenient to prepare a ZEO-1 sample containing exclusively Brønsted acid sites to precisely determine the pyridine extinction coefficient. Given that the majority of the EFAL species consists of monomeric species that are positively charged, we explored ion exchange with ammonium chloride (see experimental section), which demonstrated its effectiveness in removing the EFAL and obtaining ZEO-1 with exclusively tetrahedral Brønsted acid sites, as demonstrated by ^{27}Al NMR in Figure 3.

2D ^{27}Al multiple quantum magic angle spinning (MQMAS) experiments allowed us to distinguish at least three probable nonequivalent Al sites, Figure 4B. Then, the 1D spectrum (Figure 4A) was fitted using the Czjeck model available in Dmfit software[29]. The three peaks used reflect the location of Al in at least three angular configurations within all the available tetrahedral (T) sites. Note that 21 T sites are available for Al in the cage of ZEO-1. Based on the correlations already found between the T-O-T angles and the isotropic chemical shifts[30], it is possible to assign the observed peaks to three groups of tetrahedra (Table S1). Upon calcination, three aluminum distributions are still observed (see the ^{27}Al MQMAS shown in Figure S13) and are centered at 54.8, 58.4, and 61.6 ppm.

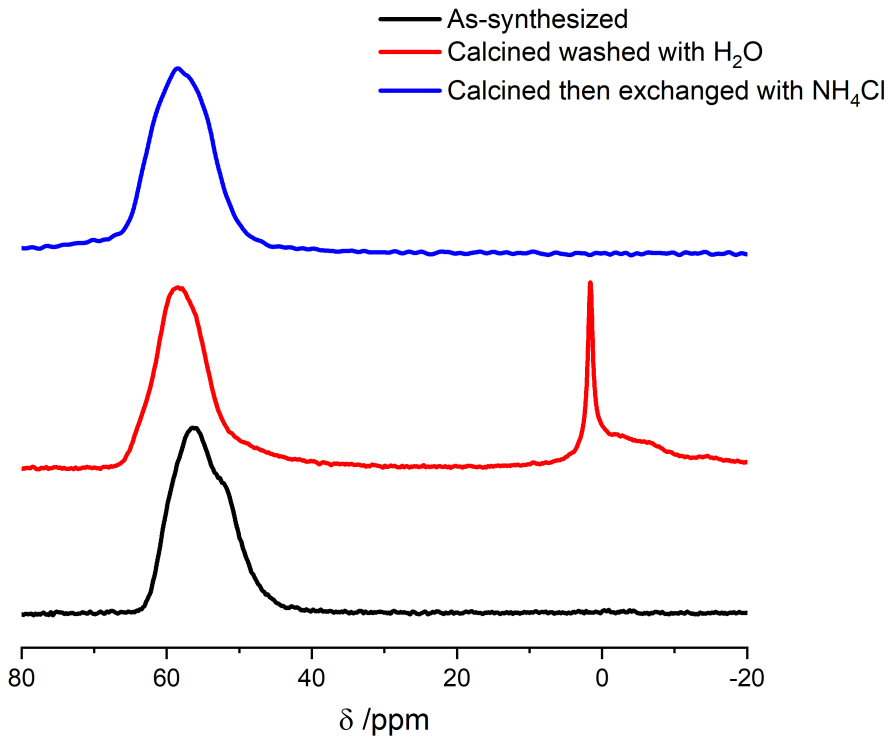

Figure 3: ^{27}Al solid-state NMR for ZEO-1: as-synthesized, calcined then washed with H_2O, and calcined then exhanged with NH_4Cl .

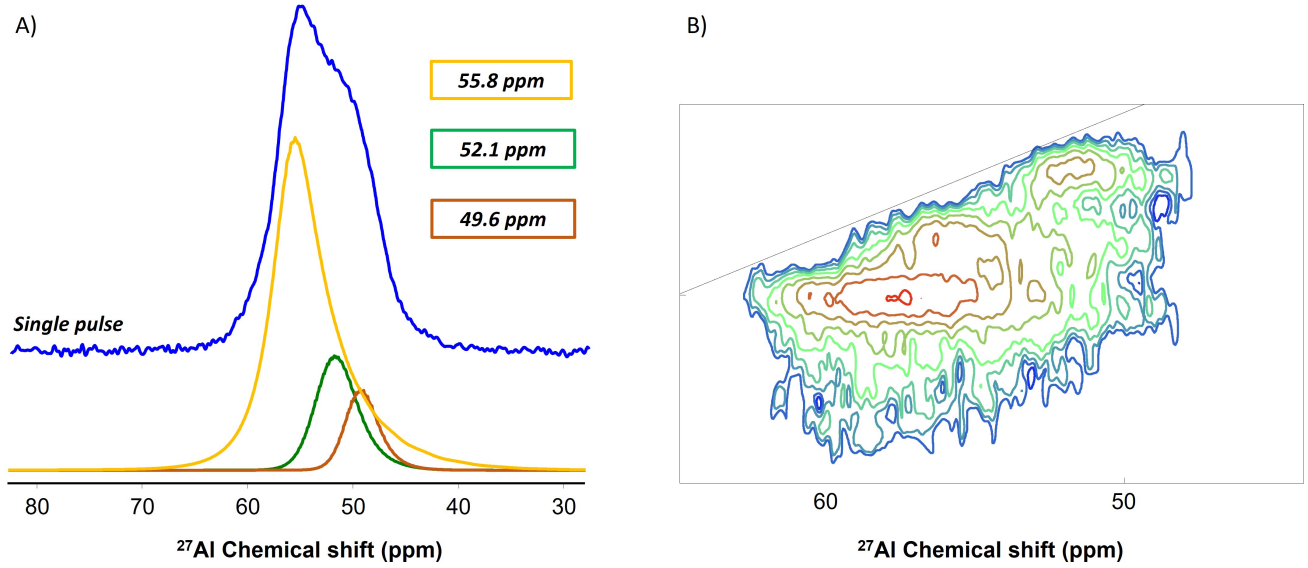

Figure 4: (A) The 1D ^{27}Al NMR fitted using the Czjeck model, and (B) the ^{27}Al MQMAS solid-state NMR for an as-synthesized ZEO-1.

3.2.3 ^{31}P NMR

ZEO-1 is synthesized using tricyclohexylmethyl phosphonium as an SDA. The liquid ^{31}P NMR spectrum presented in Figure S14 displays a single spectral line at δ= 33.9 ppm for the synthesized SDA and perfectly agrees with the solid-state ^{31}P NMR spectrum of as-synthesized ZEO-1. This agreement confirms the presence of the SDA occluded in ZEO-1 without any degradation. Figure S15 illustrates that upon calcination, the peak at δ= 33.9 ppm vanishes, giving rise to a sharp peak at 2 ppm and a series of spectral bands between -5 and -20 ppm. These changes correspond to the residual phosphorus resulting from the oxidation of the SDA.

Significant efforts have been dedicated to investigating and elucidating the nature of the phosphorus interaction with the aluminosilicate zeolite framework, notably for zeolite-Y[31] and ZSM-5[32–39]. The sharp peak at 2 ppm has been assigned to monomeric phosphate species (PO_4^{3-}), similar to those found in orthophosphoric acid. The peaks located between -5 and -12 ppm correspond to the end and middle groups of pyrophosphates or short-chain polyphosphates[40,41]. This assignment is further supported by observing that upon washing after calcination with only purified water, the peak at 2 ppm disappears, while the intensity of the peaks between -5 and -12 ppm significantly decreases. As for the spectral lines located at -19 ppm, these can be attributed to amorphous aluminophosphate units resulting from the interaction between the remaining phosphorus species and the extra-framework aluminum generated from calcination[42–44]. This interpretation is further supplemented by the complete removal of residual phosphorus species after ion exchange with ammonium chloride, which caused the removal of extra-framework aluminum.

3.2.4 ^{1}H NMR

^{1}H NMR has proven to be a valuable technique for distinguishing between hydroxyl groups, i.e., silanols and Brønsted acid sites within the zeolitic material. It also provides insights into possible hydrogen bonding interactions between these groups[45–49]. The ^{1}H NMR spectrum was recorded for a calcined sample of ZEO-1 (washed with that has been washed with H_2O) and is shown in Figure S16 to understand the aspect of the different hydroxyl groups within the ZEO-

1 framework. The spectral lines within the 0 to 2 ppm range correspond to free silanols (non- or weakly hydrogen bonded), constituting approximately 70% of the overall hydroxyl group population. Additionally, spectral lines at 3.44 and 3.66 ppm are assigned to Brønsted acid sites located on the oxygen bridging between a silicon atom and an aluminum atom, accounting for approximately 10% of the total hydroxyl group population. Furthermore, at relatively higher chemical shifts, ranging from 4 to 8 ppm, a series of broad peaks can be attributed to hydrogen-bonded hydroxyl species compromising 23% of the total hydroxyl group population. These species may involve hydrogen-bonded silanols interacting among themselves or hydrogen-bonded with Brønsted acid sites.

3.3 *In situ* infrared spectroscopy

All the ZEO-1 samples investigated by *in situ* infrared spectroscopy were synthesized under the following conditions: Si/Al = 25 | Si/SDAOH = 3 | Si/F = 20 | H_2O/Si = 7 at 190 °C using aluminum isopropoxide as an aluminum precursor. The as-synthesized ZEO-1 was then calcined at 600 °C, then exchanged with NH_4Cl, and analyzed by N_2 adsorption to give a t-plot micropore volume of 0.31 cm^3/g.

3.3.1 Interaction of pyridine and DTBPY with ZEO-1

Figure 5 displays different IR spectra in the hydroxyl group stretching vibration region for a calcined ZEO-1 sample that has undergone exchange with NH_4Cl, aiming to understand the behavior of Brønsted acid sites with minimal interference from extra-framework aluminum (EFAL). Detailed experimental protocols and technical information are available in the supporting information.

Beginning with the reference spectrum obtained after the removal of guest molecules (H_2O and NH_4^+) from the ZEO-1 framework, three distinct vibrational bands are observed. Two sharp bands are situated at 3740 and 3640 cm^{-1}, while a broader, less intense band falls between 3590 and 3490 cm^{-1}. As with all zeolites, the 3740 and 3640 cm^{-1} bands correspond to external silanols and Brønsted hydroxyl groups, respectively. As for the broadband between 3590 and 3330 cm^{-1}, may result from hydrogen bonding interactions between the internal silanols themselves, the so-called silanol nests[50–53] or with the bridging hydroxyl groups[17,54], or a mixture of both.

Pyridine (⌀= 5.5 * 5.5 Å) serves as the primary probe molecule for distinguishing between silanols and Brønsted acid sites while probing the acidity of this material and evaluating the accessibility of the latter. Following pyridine diffusion and desorption at 200 °C, the band located at 3640 cm^{-1} completely disappears, along with the ill-defined band at 3550 cm^{-1}, thus confirming their acidic character and full accessibility. Meanwhile, the band at 3740 cm^{-1} remains unaffected, albeit with a slight perturbation likely attributed to the close proximity of pyridinium ions.

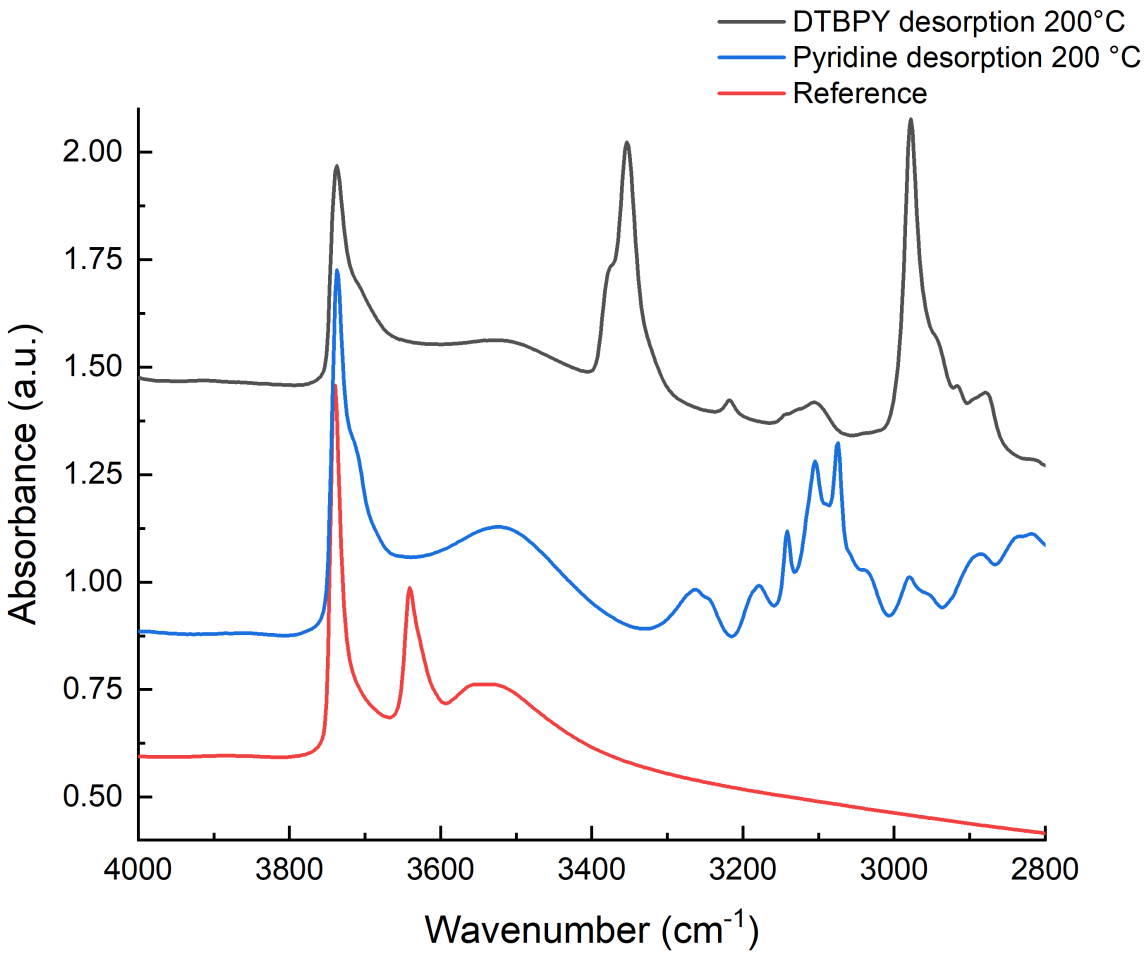

Figure 5: Infrared spectrums showing the hydroxyl group stretching vibration region for ZEO-1 calcined then exchanged with NH_4Cl after activation (Reference) and after the diffusion and desorption of pyridine and DTBPY at 200 °C.

While ZEO-1 features a more open framework relative to FAU and lacks inaccessible cages that would promote hydrogen bonding between bridging hydroxyl groups, the low-frequency vibration of this band may be due to hydrogen bonding between bridging hydroxyl groups pointing toward five-membered rings in ZEO-1, similar to what has been recently reported by Schroeder and co-workers[55].

2,6-Di-tert-butylpyridine (DTBPY) is a basic probe molecule, mainly employed for quantifying surface and pore mouth-located Brønsted acid sites in 10-membered ring zeolites and 12-membered ring zeolites, owing to its bulky geometry ($\varnothing$= 8 * 4.5 Å)[56–59]. An exception to this trend is observed with Zeolites Y[60] and Beta (BEA)[61,62], where it has been demonstrated that

the majority of Brønsted acid sites within the micropores are accessible to this probe molecule.

As depicted in Figure 5, DTBPY exhibits full accessibility to all Brønsted acid sites in ZEO-1, evident from the disappearance of vibration bands at 3640 and 3550 cm^{-1} and the emergence of a band between 3400 and 330 cm^{-1}. This characteristic peak corresponds to the N-H^+ stretching band for the 2,6-Di-tert-butylpyridinium complex formed by Brønsted hydroxyl groups. The intensity of the silanol vibration band at 3740 cm^{-1} is notably reduced and broadened, indicating a strong interaction with chemisorbed DTBPY. Furthermore, the broad vibration band attributed to silanol nests between 3630 and 3330 cm^{-1} remains evident.

3.3.2 Quantifying the number of acid sites using pyridine and DTBPY

Adapting the Beer-Lambert-Bouguer method for solid-state chemistry (see supporting information) allows the determination of the extinction coefficient for basic probe molecules to quantify the concentration of Brønsted or Lewis acid sites within zeolites.

A crucial condition for determining the extinction coefficient for pyridine is to work with a zeolite containing exclusively Brønsted acid sites. This ensures that the cumulative number of moles of pyridine adsorbed onto the zeolite can be solely attributed to the band at 1545 cm^{-1}, as pyridine interacting with Lewis acid sites will absorb at 1450 cm^{-1}. As mentioned earlier, the characterized sample is devoid of EFAL and residual phosphoric species, as observed by ^{27}Al and ^{31}P solid-state NMR, respectively, which are associated with Lewis acid sites.

Figure S17 presents a plot of the band area at 1545 cm^{-1} versus the cumulative number of moles of pyridine chemisorbed on ZEO-1, along with the stretching vibration band for the pyridinium rings at 1545 cm^{-1}.

Despite the sample being free of any EFAL and phosphorus species, as previously mentioned, a broad, low-intensity band is observed at 1450 cm^{-1}, characteristic of Lewis acid sites. This band arises from remaining traces that are undetectable by solid-state NMR. The integrated area for the band at the final point of cumulative pyridine chemisorbed corresponds to 0.5 x 10^{-5} mmol/gram (using the extinction coefficient for EFAl species reported by Zholobenko et al.[63] which is independent of the zeolite framework type), compared to 9.6 x

Table 3: The concentration of framework aluminum was obtained using Py and DTBPY adsorption using infrared spectroscopy.

Probe molecule	Si/Al ratio from ICP	$\Sigma Al_{Brønsted}$ [mmol/g]
Pyridine	24.4	0.65
DTBPY	24.4	0.60

10^{-5} mmol/g for the band at 1545 cm^{-1}, confirming the negligible amount of these Lewis acid sites.

The experiment to determine the extinction coefficient for the band at 1545 cm^{-1} has been repeated three times, yielding an excellent correlation factor, as can be seen in Figure S17. The obtained value for the extinction coefficient is $\varepsilon_{1545} = 0.9 \pm 0.023$ cm.μmol^{-1}. Figure S18 illustrates the gradual disappearance of the vibrational bands at 3640 cm^{-1} and 3550 cm^{-1} due to titration by pyridine. In the same work[63], Zholobenko et al. surveyed all the reported pyridine extinction coefficients for different zeolitic materials (see Table 1 in the cited reference). The noticeable discrepancy in the extinction coefficient values reported even for the same type of zeolite by different research groups is mainly due to the limitations resulting from the technical aspect of the used apparatus and experimental protocol. Nevertheless, the extinction coefficient we obtained is still within the reasonable value limits obtained for other zeolites.

Table 3 summarizes the concentration of Brønsted acid sites for the analyzed sample of ZEO-1 using pyridine and DTBPY. From inductive-coupled plasma analysis (ICP), the Si/Al ratio is 24.4, which is based on the amount of tetrahedral aluminum present in the framework as there are no EFAL species in the sample, according to Figure 3. The concentration of Brønsted acid sites using the determined extinction coefficient of pyridine results in 0.65 mmol/g. For DTBPY, when employing the molar extinction coefficient for the N-H^+ band (5.22 cm.μmol^{-1}) reported previously[60] for Faujasite zeolite, we observed a value of 0.60 mmol/g, which is slightly lower than that of pyridine.

To further investigate the nature of hydroxyl groups associated with the spectral region between 3630 and 3330 cm^{-1}, ZEO-1 was transformed into its cesium form (refer to the ex-

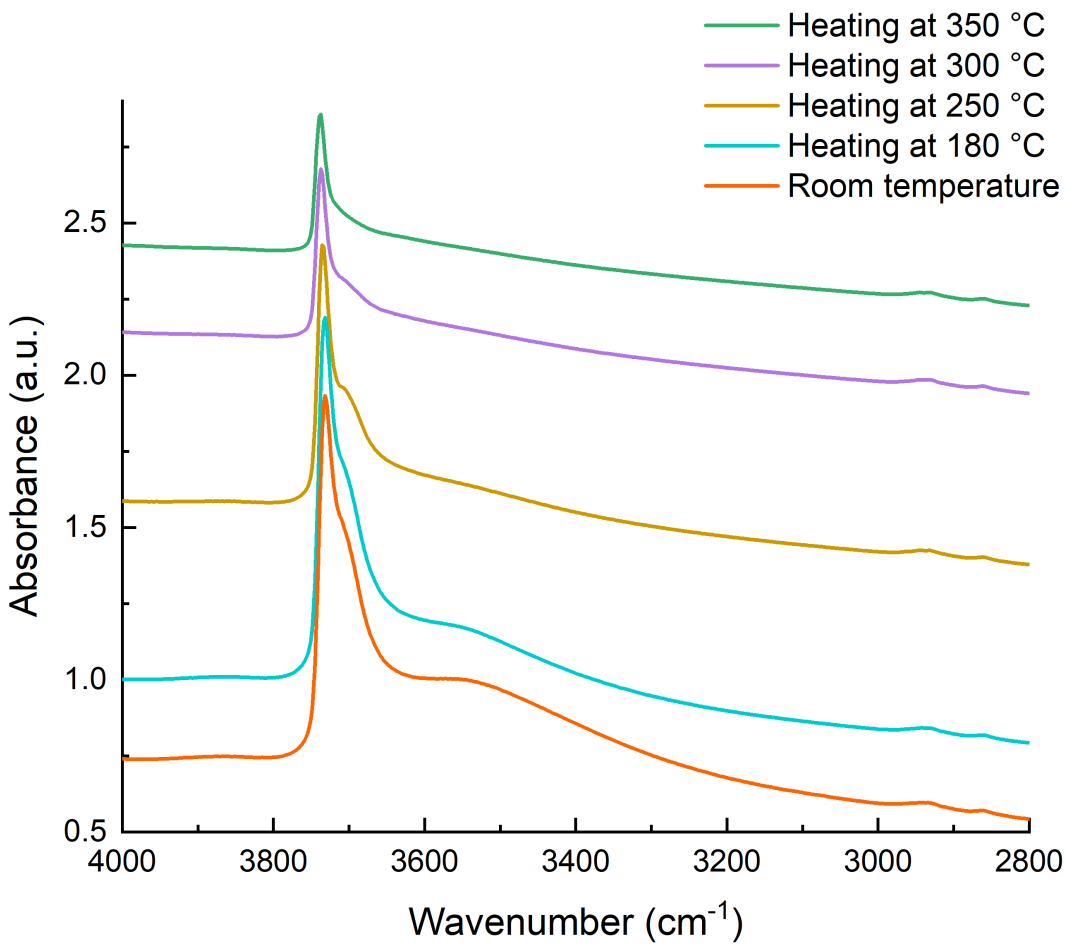

Figure 6: Infrared spectra showing the hydroxyl group stretching vibration region for ZEO-1 calcined, then exchanged with NH_4Cl, then converted to Cs-form after heating at different temperatures.

perimental section information for details) and subjected to IR spectroscopic analysis. When the protons within ZEO-1 are fully exchanged with cesium cations, the vibrational bands corresponding to the Brønsted hydroxyl must disappear as they no longer exist. In Figure 6, it is evident that under vacuum conditions (10^{-6} torr) at room temperature, the bands at 3640 and 3550 cm^{-1} are absent (see Figure S19 comparing the reference for protonic and cesium reference spectra of ZEO-1), having been completely replaced by Cs ions. Meanwhile, the silanol band at 3740 cm^{-1} shows slight perturbation, likely due to residual water within the zeolite.

Additionally, the broad band spanning from 3630 to 3330 cm^{-1} remains discernible. Upon heating at 180 °C for 5 minutes to eliminate residual water, the silanol band exhibits reduced

perturbation, while the intensity of the broadband between 3630 and 3330 cm^{-1} experiences a slight decrease. Further heating to 350 °C results in a significant transformation of the spectrum where the broad band between 3630 and 3330 cm^{-1} completely vanishes, and the intensity of the silanol band decreases notably.

This observation aligns with the thermal gravimetric analysis profile presented in Figure S20 for this sample, where a substantial weight loss (17.8%) occurs at 180 °C, attributed to water removal. Another minor weight loss (2.11%) is observed, which, in this case, corresponds to the condensation of hydroxyl groups, as the sample is in the Cs-form. Consequently, this weight loss cannot be attributed to other guest molecules.

These findings conclude that the hydroxyl groups responsible for this spectral region originate from silanol nests actively involved in hydrogen bonding. Our group has recently reported the healing of these silanol nests in the presence of Cs for chabazite zeolite, where an increase in Cs content at the expense of potassium (K) promoted the healing of silanols[64]. Furthermore, the persistence of these nests when ZEO-1 is activated in its protonic form suggests that they are stabilized by hydrogen bonding with neighboring Brønsted acid sites, resulting in the lower wavenumber shift of these Brønsted acid sites.

3.3.3 Carbon monoxide as a weak base probe molecule

Carbon monoxide (CO) is a weak base probe molecule widely utilized for distinguishing and evaluating the strength of various hydroxyl groups within the zeolite framework[56,65]. CO exhibits exceptional sensitivity to the local electrostatic field of hydroxyl groups within zeolites due to hydrogen bonding interactions via its carbon moiety. This interaction results in a shift in the vibrational frequency of the hydroxyl groups ($\Delta\nu$ OH) towards lower wavenumbers. Consequently, the magnitude of the shift directly correlates with the acidic strength of the hydroxyl group[66]. A higher $\Delta\nu$ OH indicates a stronger acid site, and the cumulative number of shifts indicates the various types of acid sites present.

In Figure 7, the impact of CO adsorption on ZEO-1 at 77 K is demonstrated following the successive introduction of discrete mono doses (ranging from 0.5 to 2 micromoles) into the cell.

The spectra recorded after each dose and the difference spectra relative to the reference spectrum are provided in the supporting information (see Figure S21). It is worth noting that CO analysis was conducted on a calcined ZEO-1 sample that had only been washed with distilled water, thus containing extra-framework aluminum (EFAL) species. Consequently, the vibration band at 3670 cm^{-1} corresponds to hydroxyl groups associated with EFAL species[67]. As for the band at 3790 cm^{-1}, it has been previously observed in γ-alumina samples and attributed to isolated hydroxyl groups[68,69]. Since this band was absent in the reference spectrum for EFAL-free samples (Figure 3), it is reasonable to assign it likewise to hydroxyl groups of EFAL species. Figure 7 reveals that the bands corresponding to acidic hydroxyl groups at 3640 and 3550 cm^{-1} experience three significant shifts towards lower wavenumbers upon interaction with CO ($\Delta\nu$ OH = 351, 231, and 137 cm^{-1}). The stretching vibration for CO molecules adsorbed on ZEO-1 is observed at 2179 cm^{-1}. This indicates the presence of three distinct types of Brønsted acid sites with varying strengths, which correlates well with the findings of ^{27}Al MQMAS, and ^{1}H NMR.

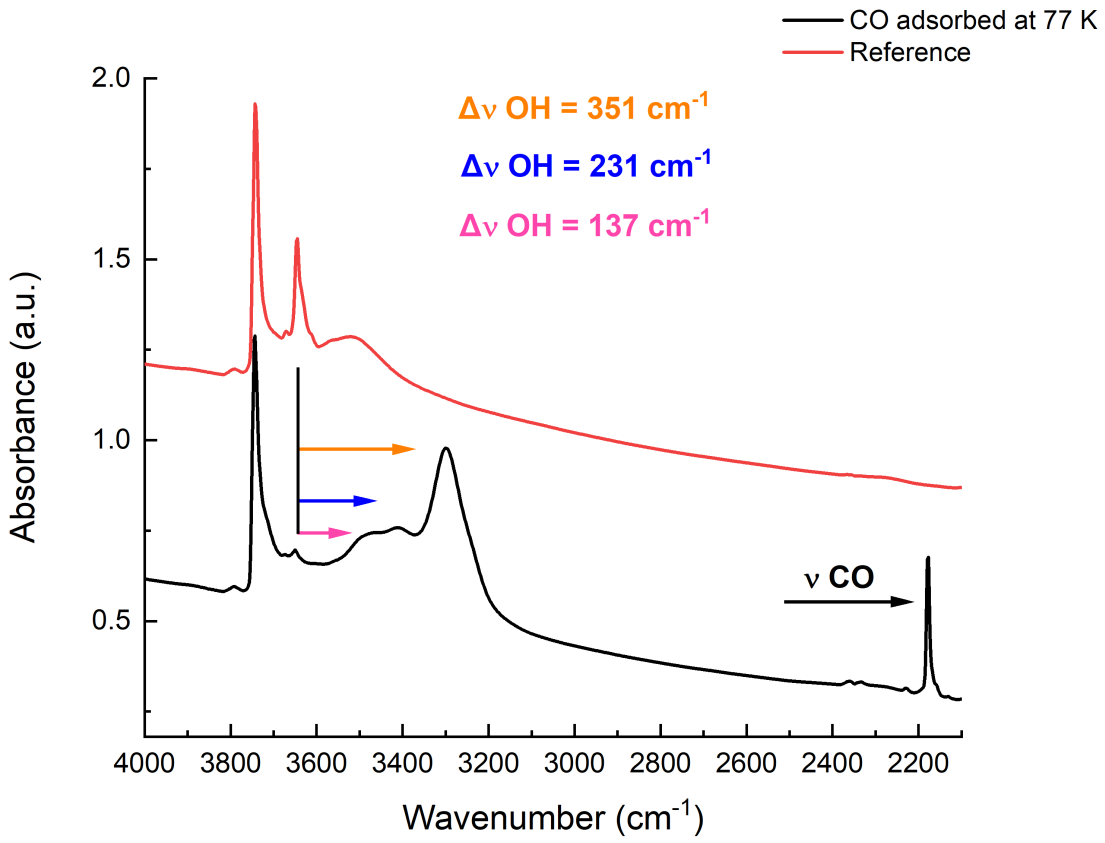

Figure 7: Infrared spectrums for a calcined ZEO-1 then washed with H_2O before and after carbon monoxide adsorption at 77 K.

3.4 DFT modeling

We used density functional calculations of a periodic ZEO-1 model to estimate the relative stability of aluminum in different T atom positions.

The results for the relative stability of the structures are shown in the left part of Table S2. For the deprotonated anionic model, the most stable position for Al substitution is T11, followed by T7 (11.1 kJ/mol less stable) and T6 and T12 (by ca. 16 kJ/mol less stable than T11), and their location is highlighted within the ZEO-1 framework in Figure 8. The least stable positions are T8, T9, and T14, which are by 42 – 46 kJ/mol less stable than the reference structure. The calculated relative energies are also presented with red triangles in Figure S22.

Among the 84 neutral models with bridging hydroxyls next to the Al centers, the most stable structure is again for Al in the T11 position, denoted as Al-T11-OHa, but the structure Al-T11-OHb is by only 3.5 kJ/mol less stable. The models with Al in position T7 are again among the most stable ones; see Al-T7-OHa, Al-T7-OHb, and Al-T7-OHc, which are by 0.6, 5.0 and 8.9 kJ/mol less stable than the most stable model. In those calculations, two other relatively stable models appear with Al in T21 and T6, namely models Al-T21-OHa and Al-T6-OHd (by 3.3 and 7.9 kJ/mol less stable than the reference structure). On the other hand, some of the models show higher relative energy up to 60 kJ/mol (see positions T8, T9, T17). The calculated relative energies of all neutral structures are shown as blue circles in Figure S22. Although, in general, the models with a more stable Al position in the deprotonated anionic structure are more stable as neutral structures, there is no strict correlation between those values since the stability of the neutral structures is affected by additional factors – formation and strength of hydrogen bonds and local distortions of the zeolite framework due to those hydrogen bonds. These two additional factors likely cause larger variations in the relative energies of the neutral structure compared to the anionic ones.

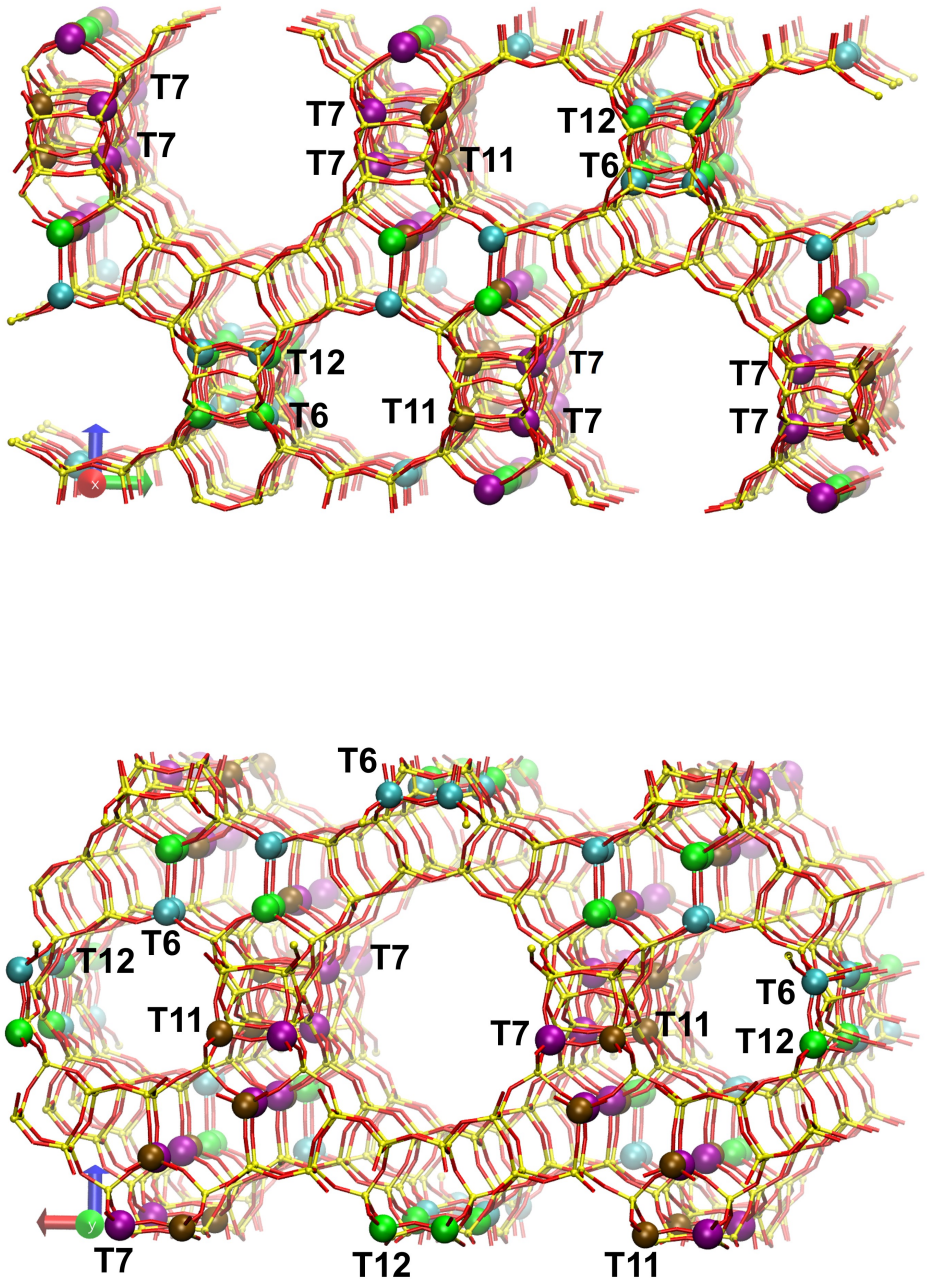

Figure 8: A schematic illustration thoughtfully delineating the positions of the most stable T-atoms, including T6 (Cyan), T7 (Pink), T11 (Brown), and T12 (Green), within the optimized anionic framework of ZEO-1, as determined by DFT modeling. This visual representation is provided for both the (Top) x-axis and (Bottom) y-axis orientations.

Using Boltzmann distribution, we calculated a tentative distribution of 25 Al (corresponding to a Si/Al ratio of 23.95) among different T-atom sites. The results are shown in the right part of Table S2 and Figure S23. The calculation with the values for the anionic structures, which may be considered representative of an as-synthesized system, suggest a strong preference for the T11 position, 21.8 of all 25 Al per unit cell (there are 32 equivalent T11 positions in one unit cell). Next is T7 with 1.5 Al (i.e., 1 or 2) in this position, followed by T6 and T12 with lower probability.

When the calculation of the Al distribution is based on the calculated relative energies of the neutral structures (at 300 K and 500 K), the results are somewhat different. The most preferable position is again T11 but with fewer Al in this T site - 12 or 9 (at 300 K and 500 K, respectively). The fraction of sites with Al in T7 increases to 9 or 8 at 300 and 500 K, respectively. The calculations suggest that 3 Al ions may be located at T21 and one in some of the positions T6 and T1, as the other positions are with minor probability.

Using the calculated energies of the optimized neutral and anionic structures, we calculated the deprotonation energies (DPE) of all bridging hydroxyl groups. The relative DPE values are calculated with respect to the structure with the lowest DPE, i.e., the most acidic hydroxyl. Interestingly, the most acidic bridging hydroxyl is Al-T11-OHd, which is one of the OH groups at the most stable Al position, T11; however, this hydroxyl is by 27.4 kJ/mol less stable than the most stable hydroxyl, Al-T11-OHa. The relative DPE values calculated for hydroxyls at all Al positions are shown in Figure S24A, while in Figure S24B, we presented the same values versus the relative stability of the same hydroxyl. In both panels, we highlighted the points for Al in the three most stable positions, T11, T7, and T21, which also feature some acidic hydroxyls. The relative DPE spreads over 50 kJ/mol as the most acidic sites (with relative DPE below 10 kJ/mol) are for Al positions T11, T16, T17, T8, and T21. There are also several hydroxyls with Al in other T sites with relative DPE between 10 and 20 kJ/mol.

As shown in Figure S24B, there are no points in the rectangular 0-20 kJ/mol on each axis (shown with black outline); namely, there are no hydroxyls, which are simultaneously among the most stable and the most acidic ones. This is not surprising since the most stable hydroxyls

typically participate in hydrogen bonds which can be estimated to contribute to their stabilisation with about 20 kJ/mol. On the other hand, the most acidic bridging hydroxyls should not participate in hydrogen bonds and point towards zeolite channels; thus, they are less stable.

Although one hydroxyl may not be simultaneously stable and most acidic, at one Al position, Al-T11, we have one most stable and one most acidic hydroxyl, OHa and OHd, respectively. Thus, upon interaction with guest molecules, the proton may move from OHa to OHd or OHc, which is also among the most acidic ones. A similar combination of stable OH and acidic OH is observed at the T7 and T21 positions of Al. If we consider the relative stability of the Al substitution in the anionic structure, the model Al-T16-OHc may also be feasible since it has a relative DPE value of 5 kJ/mol and the structure Al-T16 is by 19.8 kJ/mol less stable than the reference one, Al-T11.

Both the anionic and neutral models suggest a preference for aluminum location at the T11 position, which is exposed at the 12-membered ring but not to the 16-membered ring. The next preference for Al substitution is T7 at the 16-membered ring channel. The other T-sites where Al may be located with lower probability, T6 and T21, are also at the 12-membered ring channel, but T1 is at the 16-ring channel. The least stable sites for Al substitution, T8, T9, T14, and T17, are located at the 16-membered ring channels at the channel intersection, where the Al site will be the most accessible. Note, however, that the presence of the template in the zeolite channels during the synthesis of the samples may influence to some extent the preferable crystallographic positions for aluminum in the framework, as shown both for aluminum and for other T atoms.[70,71]. The most acidic hydroxyls are also at the T11 position of Al, followed by T16, T17, T8, and T21. As shown above, T8 and T17 are among the least stable positions for Al substitution, and Al is unlikely to be present in those sites.

As such, considering the optimized structures obtained with DFT modeling, the ^{27}Al MQ-MAS NMR spectra, and the correlations already established between the chemical shifts and the TOT angles, we may potentially assign the three Al populations mainly present in the 12-membered ring channels, i.e., T6 (12 MR), T7 (16 MR), T11 (12 MR) and T12 (12 MR), they correspond to three T-O-T angular configurations respectively. When considering the DFT cal-

culations, these sites are among the most stable T sites. Furthermore, the sites exclusively present in 16 MR channels, i.e., T1, T3, T4, T8, T9, and T10, are energetically among the less favorable sites.

3.5 Catalytic tests

We completed our acidity study with three test reactions, which are the alkylation of phenol with tert-butyl alcohol, *n*-hexane cracking, and anisole transformation, to evaluate the potential of ZEO-1 as a heterogeneous catalyst compared to two commercial zeolites (purchased from Zeolyst) used in different industrial processes, which are zeolite Beta (***BEA** CP814E*) and Ultra Stable Y (USY: CBV 712) zeolite with **FAU** topology. The ZEO-1 sample used for the catalytic tests is from the scaled-up batch discussed above that was calcined and then exchanged with ammonium chloride to remove residual phosphorus species and reduce the EFAL species. Accordingly, it is possible to evaluate the catalytic performance exclusively for the Brønsted acid sites without any contribution from other species. The experimental and technical details for the catalytic tests are provided in the experimental section. The three zeolites' physicochemical properties and catalytic test results are presented in Table 4.

3.5.1 Alkylation of phenol with tert-butyl alcohol

The phenol alkylation with tert-butyl alcohol is a classical Friedel-Crafts alkylation reaction catalyzed by the intrinsic acid sites of zeolite catalysts. This reaction typically yields three distinct products: ortho-butyl phenol (*o*-TBP), para-butyl phenol (*p*-TBP), and 2,4-di-tert-butyl phenol (2,4-DTBP). The selectivity for these products is significantly influenced by the available pore volume, which is determined by the pore opening and geometry directly associated with the presence of acid sites in this environment[72–74].

Figure 9 presents the selectivity percentages of the three products (*o*-TBP, *p*-TBP, and 2,4-DTBP) obtained using ZEO-1, BETA, and USY where the percent of conversion for the three zeolites was 84, 71, and 90%, respectively using a batch reactor. USY shows almost no selectivity towards any of the three products, with comparable percentages yielding approximately 37% of *o*-TBP and 2,4-DTBP, and nearly 26.11% of *p*-TBP. Conversely, zeolite Beta exhibits strong selectivity towards *p*-TBP, with around 87% selectivity and almost negligible selectivity towards 2,4-DTBP (3%) and roughly 11% towards *o*-TBP.

This highlights the significant influence of pore volume and geometry on the selectivity of

the conversion process. For USY, its spacious micropore volume of the super cage (approximately 1.2 nm), along with induced mesoporosity due to steaming, results in no shape selectivity effect as the kinetic diameters of all three possible products can comfortably fit within the pore system of USY. In contrast, the constrained 12-membered ring channels of zeolite Beta cannot accommodate the bulky geometry of 2,4-DTBP and appear to align well with the linear conformation of p-TBP rather than the non-linear conformation of o-TBP, thus promoting its formation within its channels.

Interestingly, ZEO-1 shows comparable product selectivity to zeolite Beta, yielding slightly lower and higher percentages of p-TBP (approximately 76% and 17%, respectively) and around 7% of *o*-TBP. Despite possessing a supercage formed by the intersection of 16-MR, whose dimension is around 1.1 nm comparable to that of USY, we observe that ZEO-1 exhibits much higher selectivity towards *p*-TBP rather than 2,4-DTBP. This suggests that the majority of the acid sites within ZEO-1 are preferentially located within the 12-MR channels. However, simultaneously, the amount of 2,4-DTBP remains slightly higher than that of zeolite Beta, most likely due to catalytic activity within the 16-MR super cages. Moreover, this correlates well with the DFT modeling findings, which suggest that three out of the most stable tetrahedral sites for aluminum substitution (T6, T11, and T12) are located within the 12-MR channels, while only one site is probably located in the 16-MR channel (T7).

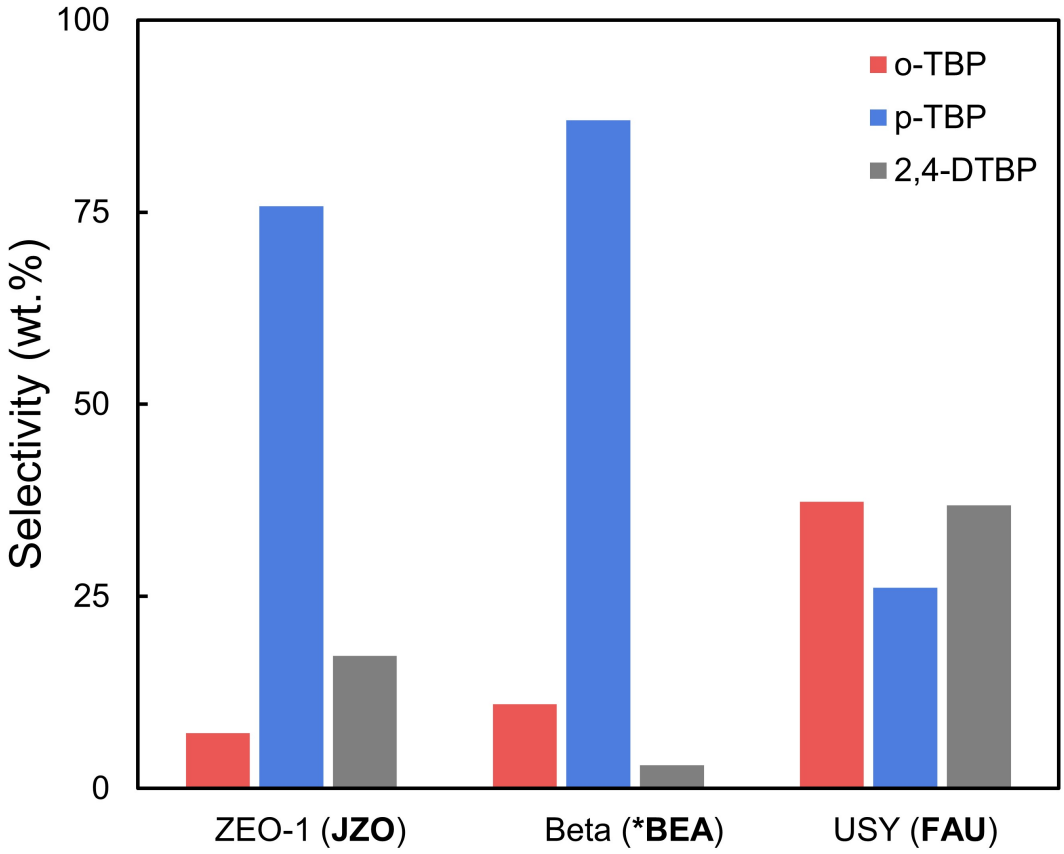

Figure 9: Product selectivity during phenol alkylation by tert-butyl alcohol over ZEO-1, Beta, and USY zeolites.

3.5.2 *n*-hexane cracking

The cracking of *n*-hexane is a well-known model reaction commonly employed to assess the acidity of zeolites[75]. This reaction's suitability arises from the remarkable stability of the C–C bond, making it an ideal means to evaluate the strength of Brønsted acid sites[76].

In Figure 10, plots of -Ln(1-X) versus W/F for the three structures are depicted, where X represents the conversion, W signifies the catalyst weight, and F denotes the mass flow of *n*-hexane. The linearity observed in these plots suggests that the kinetics of *n*-hexane cracking adhere to first-order reaction kinetics, indicative of predominant monomolecular pathway reactions. This inference is further supported by the proportionality observed between the molar yield of principal products and initial conversion[75] (see Figure S25). The activities, determined from the slopes of these linear plots, are measured at 310, 31, and 20 mmol h^{-1} $g_{cat}{}^{-1}$. Further-

more, the constancy of n-hexane conversion after 1 hour of reaction (see Figure S26) under the chosen operational conditions underscores the absence of deactivation within the first hour of testing on the evaluated catalyst.

The catalyst turnover frequency (TOF), based on activity per Brønsted acid site (refer to the experimental section), for the three zeolites is outlined in Table 4. ZEO-1 exhibits a TOF of 65 molecules per site per hour, marginally surpassing that of USY zeolite (46 molecules per site per hour) while being approximately tenfold lower than Beta (620 molecules per site per hour). The elevated activity of zeolite Beta has been attributed to the presence of considerable amounts of EFAl species within the zeolite's framework that exalts the cracking activity[75]. This comparison highlights that ZEO-1 possesses a comparable number of acid sites capable of catalyzing the proto-catalytic cracking of *n*-hexane to USY, albeit with weaker Brønsted acidity than Beta. This result assures that extra-large pore zeolites' acidic strength is at least equivalent to the horsepower of FCC catalysis being USY, which satisfies the long-foreseen anticipation for this class of materials and presents a positive sign for future applications.

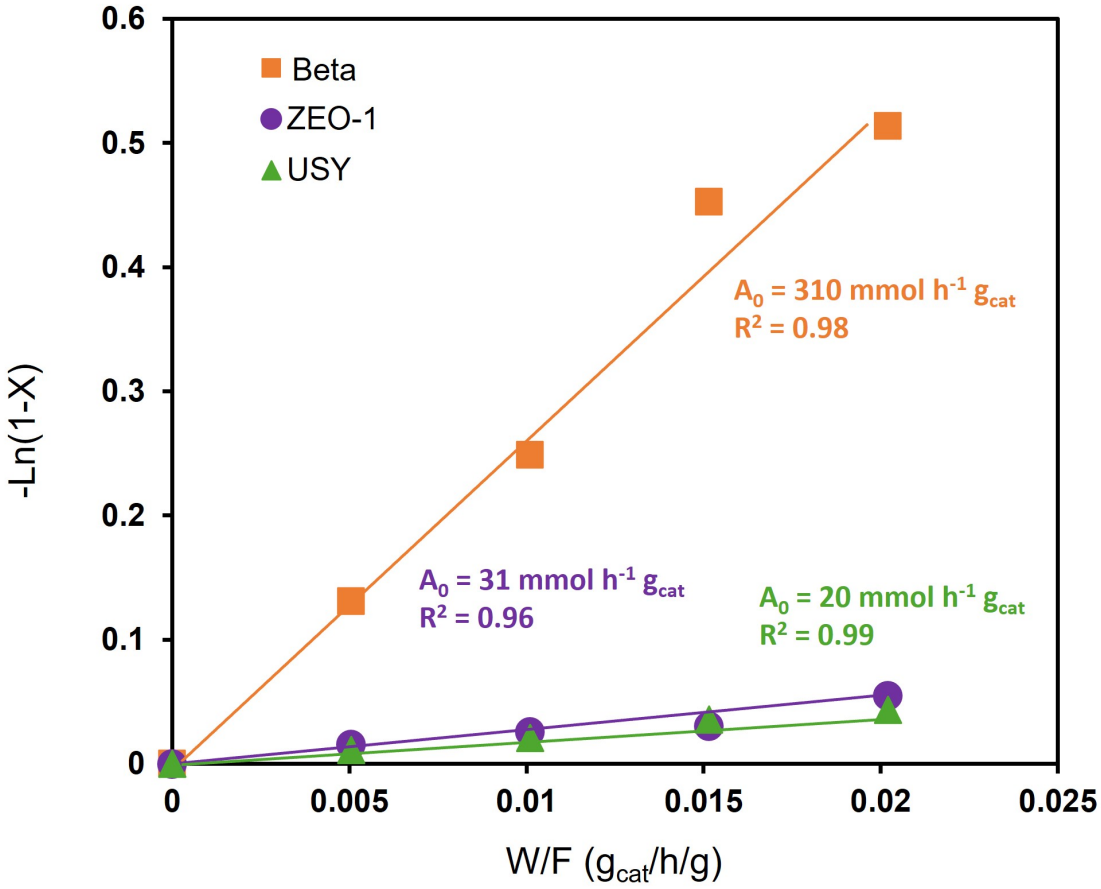

Figure 10: First-order kinetic plots of *n*-hexane cracking on ZEO-1, Beta, and USY zeolites at 540 °C.

3.5.3 Anisole disproportionation

Given the long-anticipated potential of employing extra-large pore aluminosilicate zeolites for biomass upgrading applications, believed to outperform existing large pore zeolites due to restricted pore apertures enhancing treatment of bulky molecules and diffusion profiles, a comparison of the deactivation profiles of ZEO-1 with those of Beta and USY using a biomass model reaction becomes intriguing.

Anisole disproportionation is a model reaction for the catalytic upgrading of biomass pyrolysis bio-oils[77–79]. Anisole's methoxy group and aromatic cycle are largely found in primary pyrolysis products of lignocellulosic biomass. Anisole undergoes several transalkylation reactions, first producing methylanisole and phenol, then increasingly methylated phenolics:

cresols, xylenols, mesitols (respectively methyl, dimethyl, and trimethyl phenol)[77,78].

In Figure 11, the relative activity ($\Phi = \alpha_i/\alpha_0$) versus time on stream (TOS) is presented. The study was performed at several contact times for each catalyst where the deactivation constants k_D (h^{-1}), determining the steepness of the deactivation curve for the three catalysts, are summarized in Table 4 (refer to the experimental section for details).

All three catalysts exhibit an inverse exponential deactivation pattern, with Beta and USY displaying nearly identical k_D values of 26 and 25 h^{-1}, respectively. Remarkably, ZEO-1 exhibits a significantly lower k_D value of 7 h^{-1}, approximately 3.6 times lower than its counterparts. Notably, the Beta sample utilized is ultra-nanosized with a crystal size of 30 nm (nearly 14 times smaller), accompanied by spacious mesoporosity (V_{meso} = 0.87 cm^3/g) resulting from interparticle voids. Similarly, the USY catalyst is intrinsically mesoporous due to the steaming process during its hierarchization (V_{meso} = 0.25 cm^3/g), suggesting minimal kinetic diffusion limitations for reactants/products within and out of the catalyst particles for both zeolites. In contrast, the ZEO-1 material is employed without ultra-nano dimensions ($\leq$ 100 nm) or post-synthetic hierarchization, yet it demonstrates superior stability to Beta and USY. This enhanced stability can be attributed to the limited population of acid sites within the 16-membered ring (16-MR) channels of ZEO-1, thereby facilitating a free molecular diffusion pathway and ensuring a steady performance.

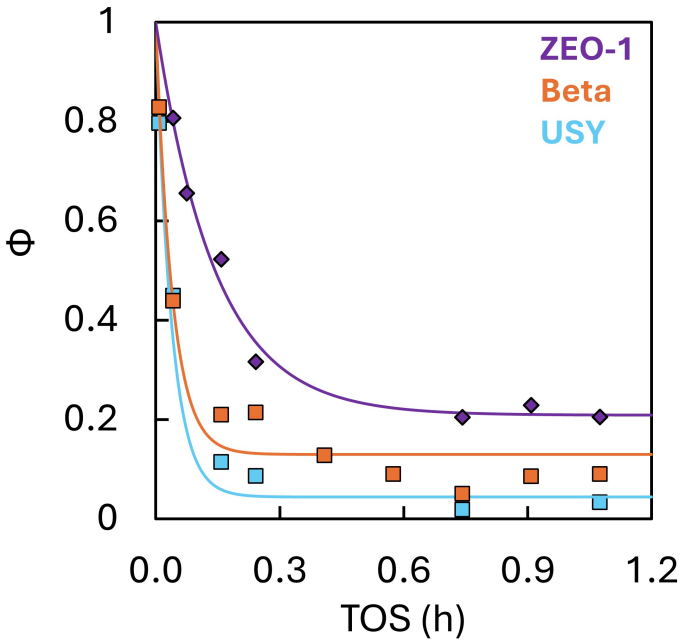

Figure 11: Evolution of activity with time on stream (TOS) for anisole disproportionation on zeolites. Dots: experimental data. Lines: deactivation modeling.

Table 4: The physicochemical properties and catalytic performance comparison of ZEO-1, Beta, and USY zeolites.

	ZEO-1 (JZO)	Beta (*BEA)	USY (FAU)
Pore network (Å)	**16** 10.62×9.41/10.54×9.64 *** ↔ **12** 7.24×6.60/7.18×5.48	**12** 6.6 x 6.7* ↔ **12** 5.6 x 5.6*	**12** 7.4 x 7.4***
Si/Al[a]	22.5	12.5	6
ΣAl$_{Brønsted}$ (mmol/g)	0.51	0.50[b]	0.54[b]
ΣAl$_{Lewis}$ (mmol/g)	0.04	0.12[c]	0.19[c]
Crystal size (nm)[d]	470	30	500
Surface area (m^2/g)[e]	973	528	762
V$_{micro}$ (cm^3/g)[f]	0.31	0.15	0.21
V$_{meso}$ (cm^3/g)[g]	0.10	0.87	0.25
Phenol alkylation with tert-butyl alcohol (at 80 °C)			
Conversion (%)	84	71	90
***n*-Hexane cracking (at 540 °C)**			
TOF (molecules per site h^{-1})	65	620	46
Anisole disproportionation (at 400 °C)			
k$_D$ (h^{-1})	7	26	25

[a] Determined from ICP analysis.
[b] Calculated using the extinction coefficient $\epsilon_{\text{Brønsted}}$ at 1545 cm^{-1} of pyridine from ref.[63].
[c] Calculated using the extinction coefficient ϵ_{Lewis} at 1450 cm^{-1} of pyridine ref.[63].
[d] Determined using SEM analysis.
[e] Apparent surface area calculated using the Roquerol BET-criteria.
[f] Micropore volume is calculated by the t-plot method using the Harkins and Jura thickness equation with a monolayer thickness range defined between 2.5 to 5 Å.
[g] Mesopore volume calculated by $V_{meso} = V_{total} - V_{micro}$, where V_{total} is the total pore volume calculated at $P/P_0 = 0.97$.

4 Conclusion

In this work, we reported a comprehensive investigation of the synthesis and the acidic properties of a 16-membered ring aluminosilicate zeolite ZEO-1.

Using sodium aluminate as an aluminum source with the optimal amount of fluoride allows for the shortest synthesis period of leaf-like and isometric micron-sized ZEO-1 crystals within only 8 days. However, using aluminum isopropoxide as an aluminum source favors the crystallization of ill-defined spherical nanosized zeolites. Using both aluminum sources, the aluminum loading of ZEO-1 shows convenient flexibility from high silica ratio to relatively high alumina ratios. The water content temperature influenced the synthesis kinetics and crystal habit of ZEO-1, while the amount of SDAOH influenced only the latter.

Using ^{27}Al NMR, we identified the potential existence of three different aluminum populations based on their angular configuration, supported by ^{1}H NMR. Then, via *in situ* infrared spectroscopy, we deciphered the acidic nature of the vibrational bands in the hydroxy group stretching vibration region using pyridine and DTBPY as probe molecules. ZEO-1 exhibits two vibrational bands corresponding to Brønsted acid sites and another broad vibrational band attributed to hydrogen-bonded silanol species that was supported by analyzing the cesium form of ZEO-1. Moreover, the extinction coefficient for pyridinium ions at the band of 1545 cm^{-1} was determined to be 0.9 $cm.\mu mol^{-1}$.

DFT modeling revealed that the most stable T-atom sites for aluminum substitution in the anionic model of ZEO-1 are at T6 (12 MR), T7 (16 MR), T11 (12 MR), and T12 (12 MR), with T11 being the most stable. Correlating the ^{27}Al NMR chemical shifts calculated using the optimized structure of ZEO-1 obtained with DFT and the chemical shifts of the three aluminum populations obtained by ^{27}Al MQMAS allowed us to assign these chemical shifts to the most stable T-atoms revealed by DFT calculations.

In the comparative analysis of catalytic performance among ZEO-1, Beta, and USY zeolites in the alkylation of phenol by tert-butyl alcohol, *n*-hexane cracking, and anisole disproportionation, ZEO-1 demonstrated a similar catalytic selectivity to zeolite Beta. This finding aligns with DFT modeling results, suggesting that most aluminum species, and hence Brønsted acid

sites, are potentially located within the 12-membered ring (12 MR) channels of ZEO-1. Moreover, the strength of the Brønsted acid sites within ZEO-1 was found to be comparable to that of USY: CBV 712, although notably weaker than those of zeolite Beta. ZEO-1 exhibited enhanced stability for anisole conversion compared to ultra-nanosized Beta and mesoporous USY zeolites, highlighting its potential for further catalytic applications.

5 Supplementary Materials

The supporting information file (https://pubs.acs.org/doi/10.1021/acs.chemmater.4c00186) includes the following:

- Technical details for the experimental setups used to characterize the physicochemical properties of ZEO-1, along with the computational details for the DFT modeling.
- PXRD, nitrogen adsorption/desorption, TGA figures, and SEM images for different ZEO-1 samples synthesized under different conditions.
- ^{29}Si, ^{27}Al (1D and MQMAS), ^{31}P, and ^{1}H solid-state NMR figures.
- In situ IR spectroscopy figures illustrating the determination of the molar extinction coefficient of the 1545 cm^{-1} pyridinium band, comparison between the protonic form of ZEO-1 and its Cs form, and the series of spectra recorded after sending discrete monodoses of CO into the IR cell.
- DFT modeling figures presenting the relative stability of the ZEO-1 structure, the calculated aluminum distribution based on the Boltzmann distribution, and the relative deprotonation energy of all the bridging hydroxyl groups versus the Al positions.
- Catalytic test result figures of the initial yields of the principal cracking products as a function of initial *n*-hexane conversion and the *n*-hexane conversion as a function of time on stream for ZEO-1, Beta, and USY.

- Two supplementary tables: Table S1 summarizes the T-O-T bond angles corresponding to the aluminum substitution for each T-atom within the ZEO-1 framework and its corresponding isotropic chemical shift, and Table S2 presents the relative stability of the modeled 21 anionic structures and 84 neutral structures with different locations of Al and of the charge-compensating proton around them.

6 Conflict of interest

The authors declare no conflict of interest.

7 Acknowledgments

MF, JF, BW, LL, and VV acknowledge the financial support from the ZeoMah – LABEX project. VV and PStP acknowledge partial financial support from the European Union-NextGenerationEU, through the National Recovery and Resilience Plan of the Republic of Bulgaria, project No. BG-RRP- 2.004-0008 and project No. BG-RRP-2.004- 0008-C01, respectively. The computational resources have been provided by Discoverer PetaSC and Eu- roHPC JU via access to the Discoverer supercomputer.

AM acknowledges the Spanish Ministry of Science and Innovation (RYC2018-024561-I) and the regional government of Aragon (DGA E13_20R). The authors acknowledge the use of instrumentation as well as the technical advice provided by the National Facility ELECMI ICTS node "Laboratorio de Microscopías Avanzadas" at the University of Zaragoza.

References

1. Corma, A. From microporous to mesoporous molecular sieve materials and their use in catalysis. *Chemical reviews* **97,** 2373–2420 (1997).

2. Vermeiren, W. & Gilson, J.-P. Impact of zeolites on the petroleum and petrochemical industry. *Topics in Catalysis* **52,** 1131–1161 (2009).

3. Verboekend, D., Nuttens, N., Locus, R., Van Aelst, J., Verolme, P., Groen, J., Pérez-Ramírez, J. & Sels, B. F. Synthesis, characterisation, and catalytic evaluation of hierarchical faujasite zeolites: milestones, challenges, and future directions. *Chemical Society Reviews* **45,** 3331–3352 (2016).

4. Smith, J. *Acido-basic catalysis application to refining and petrochemistry* (IFP Publications Oxford, Reino Unido, 2005).

5. Davis, M. E. The quest for extra-large pore, crystalline molecular sieves. *Chemistry–A European Journal* **3,** 1745–1750 (1997).

6. Zones, S. I. & Davis, M. E. Zeolite materials: recent discoveries and future prospects. *Current Opinion in Solid State and Materials Science* **1,** 107–117 (1996).

7. Davis, M. E. New vistas in zeolite and molecular sieve catalysis. *Accounts of chemical research* **26,** 111–115 (1993).

8. Davis, M. E. *Evolution of extra-large pore materials* in *Studies in Surface Science and Catalysis* **135** (Elsevier, 2001), 29–36.

9. Lobo, R. F., Tsapatsis, M., Freyhardt, C. C., Khodabandeh, S., Wagner, P., Chen, C.-Y., Balkus, K. J., Zones, S. I. & Davis, M. E. Characterization of the extra-large-pore zeolite UTD-1. *Journal of the American Chemical Society* **119,** 8474–8484 (1997).

10. Freyhardt, C., Tsapatsis, M., Lobo, R., Balkus, K. & Davis, M. A high-silica zeolite with a 14-tetrahedral-atom pore opening. *Nature* **381,** 295–298 (1996).

11. *IZA Structure Commission: Database of Zeolite Structures* `https://europe.iza-structure.org/IZA-SC/ftc_table.php`. Accessed: May 10, 2024.

12. Jiang, J., Yu, J. & Corma, A. Extra-large-pore zeolites: bridging the gap between micro and mesoporous structures. *Angewandte Chemie International Edition* **49,** 3120–3145 (2010).

13. Li, J., Corma, A. & Yu, J. Synthesis of new zeolite structures. *Chemical Society Reviews* **44,** 7112–7127 (2015).

14. Wen, J., Zhang, J. & Jiang, J. Extra-large pore zeolites: a ten-year updated review. *Chemical Journal of Chinese Universities* **42,** 101–116 (2021).

15. O'keeffe, M. & Yaghi, O. Germanate zeolites: contrasting the behavior of germanate and silicate structures built from cubic T8O20 units (T= Ge or Si). *Chemistry–A European Journal* **5,** 2796–2801 (1999).

16. Eliášová, P., Opanasenko, M., Wheatley, P. S., Shamzhy, M., Mazur, M., Nachtigall, P., Roth, W. J., Morris, R. E. & Čejka, J. The ADOR mechanism for the synthesis of new zeolites. *Chemical Society Reviews* **44,** 7177–7206 (2015).

17. Martinez-Triguero, J., Diaz-Cabanas, M., Camblor, M., Fornes, V., Maesen, T. L. & Corma, A. The catalytic performance of 14-membered ring zeolites. *Journal of Catalysis* **182,** 463–469 (1999).

18. Zones, S. I. & Chen, C.-Y. *Zeolite Me-UTD-1* US Patent 6,103,215, issued by the U.S. Patent and Trademark Office (USPTO). Aug. 2000.

19. Chen, C.-Y. & Zones, S. I. *Method for heteroatom lattice substitution in large and extra-large pore borosilicate zeolites* US Patent 6,468,501, issued by the U.S. Patent and Trademark Office (USPTO). Oct. 2002.

20. Lin, Q.-F., Gao, Z. R., Lin, C., Zhang, S., Chen, J., Li, Z., Liu, X., Fan, W., Li, J., Chen, X., *et al.* A stable aluminosilicate zeolite with intersecting three-dimensional extra-large pores. *Science* **374,** 1605–1608 (2021).

21. Willhammar, T., Burton, A. W., Yun, Y., Sun, J., Afeworki, M., Strohmaier, K. G., Vroman, H. & Zou, X. EMM-23: A stable high-silica multidimensional zeolite with extra-large trilobe-shaped channels. *Journal of the American Chemical Society* **136,** 13570–13573 (2014).

22. Smeets, S., Xie, D., Baerlocher, C., McCusker, L. B., Wan, W., Zou, X. & Zones, S. I. High-Silica Zeolite SSZ-61 with Dumbbell-Shaped Extra-Large-Pore Channels. *Angewandte Chemie International Edition* **53,** 10398–10402 (2014).

23. Meise, W. a. & Schwochow, F. *Kinetic studies on the formation of zeolite A* in *Molecular Sieves* (eds Meier, W. & Uytterhoeven, J.) (ACS Publications, 1973), 169–178.

24. Engelhardt, G. *Solid state NMR spectroscopy applied to zeolites* in *Studies in surface science and catalysis* **58** (Elsevier, 1991), 285–315.

25. Engelhardt, G., Lohse, U., Samoson, A., Mägi, M., Tarmak, M. & Lippmaa, E. High resolution 29Si nmr of dealuminated and ultrastable Y-zéolites. *Zeolites* **2,** 59–62 (1982).

26. Lippmaa, E., Maegi, M., Samoson, A., Tarmak, M. & Engelhardt, G. Investigation of the structure of zeolites by solid-state high-resolution silicon-29 NMR spectroscopy. *Journal of the American Chemical Society* **103,** 4992–4996 (1981).

27. Scherzer, J. *The Preparation and Characterization of Aluminum-Deficient Zeolites* in *Catalytic Materials: Relationship Between Structure and Reactivity* (eds Jr., T. E. W., Betta, R. A. D., Derouane, E. G. & Baker, R. T. K.) (ACS Publications, 1984), 157–200.

28. Szostak, R. *Modified zeolites* in *Studies in Surface Science and Catalysis* **58** (Elsevier, 1991), 153–199.

29. Massiot, D., Fayon, F., Capron, M., King, I., Le Calvé, S., Alonso, B., Durand, J.-O., Bujoli, B., Gan, Z. & Hoatson, G. Modelling one-and two-dimensional solid-state NMR spectra. *Magnetic resonance in chemistry* **40,** 70–76 (2002).

30. Lippmaa, E., Samoson, A. & Magi, M. High-resolution aluminum-27 NMR of aluminosilicates. *Journal of the American Chemical Society* **108,** 1730–1735 (1986).

31. Corma, A., Fornes, V., Kolodziejski, W. & Martineztriguero, L. Orthophosphoric acid interactions with ultrastable zeolite-Y: infrared and NMR studies. *Journal of Catalysis* **145,** 27–36 (1994).

32. Blasco, T., Corma, A. & Martínez-Triguero, J. Hydrothermal stabilization of ZSM-5 catalytic-cracking additives by phosphorus addition. *Journal of catalysis* **237,** 267–277 (2006).

33. Chen, N., Kaeding, W. & Dwyer, F. Para-directed aromatic reactions over shape-selective molecular sieve zeolite catalysts. *Journal of the American Chemical Society* **101,** 6783–6784 (1979).

34. Jentys, A., Rumplmayr, G. & Lercher, J. A. Hydroxyl groups in phosphorus-modified HZSM-5. *Applied catalysis* **53,** 299–312 (1989).

35. Vinek, H., Rumplmayr, G. & Lercher, J. A. Catalytic properties of postsynthesis phosphorus-modified H-ZSM5 zeolites. *Journal of Catalysis* **115,** 291–300 (1989).

36. Lercher, J. & Rumplmayr, G. Controlled decrease of acid strength by orthophosphoric acid on ZSM5. *Applied catalysis* **25,** 215–222 (1986).

37. Caro, J., Bülow, M., Derewinski, M., Haber, J., Hunger, M., Kärger, J., Pfeifer, H., Storek, W. & Zibrowius, B. NMR and IR studies of zeolite H-ZSM-5 modified with orthophosphoric acid. *Journal of Catalysis* **124,** 367–375 (1990).

38. Lischke, G., Eckelt, R., Jerschkewitz, H.-G., Parlitz, B., Schreier, E., Storek, W., Zibrowius, B. & Öhlmann, G. Spectroscopic and physicochemical characterization of P-modified H-ZSM-5. *Journal of catalysis* **132,** 229–243 (1991).

39. Zhuang, J., Ma, D., Yang, G., Yan, Z., Liu, X., Liu, X., Han, X., Bao, X., Xie, P. & Liu, Z. Solid-state MAS NMR studies on the hydrothermal stability of the zeolite catalysts for residual oil selective catalytic cracking. *Journal of catalysis* **228,** 234–242 (2004).

40. Grimmer, A.-R. & Haubenreisser, U. High-field static and MAS31P NMR: Chemical shift tensors of polycrystalline potassium phosphates P2O5· xK2O ($O \leq x \leq 3$). *Chemical physics letters* **99,** 487–490 (1983).

41. Duncan, T. & Douglas, D. On the 31P chemical shift anisotropy in condensed phosphates. *Chemical physics* **87,** 339–349 (1984).

42. Decanio, E. C., Edwards, J. C., Scalzo, T. R., Storm, D. A. & Bruno, J. W. FT-IR and solid-state NMR investigation of phosphorus promoted hydrotreating catalyst precursors. *Journal of catalysis* **132,** 498–511 (1991).

43. Blackwell, C. & Patton, R. Aluminum-27 and phosphorus-31 nuclear magnetic resonance studies of aluminophosphate molecular sieves. *The journal of physical chemistry* **88,** 6135–6139 (1984).

44. Müller, D., Jahn, E., Ladwig, G. & Haubenreisser, U. High-resolution solid-state 27Al and 31P NMR: correlation between chemical shift and mean Al-OP angle in AlPO4 polymorphs. *Chemical physics letters* **109,** 332–336 (1984).

45. Engelhardt, G. & Michel, D. *High-resolution solid-state NMR of silicates and zeolites* (John Wiley and Sons, New York, NY, 1987).

46. Freude, D. *High Resolution Solid-State 1H Nmr Studies of Zeolites* in *Studies in Surface Science and Catalysis* **52** (Elsevier, 1989), 169–192.

47. Jacobs, W., De Haan, J., Van de Ven, L. & Van Santen, R. Interaction of ammonia with Broensted acid sites in different cages of zeolite Y as studied by proton MAS NMR. *The Journal of Physical Chemistry* **97,** 10394–10402 (1993).

48. White, J. L., Beck, L. W. & Haw, J. F. Characterization of hydrogen bonding in zeolites by proton solid-state NMR spectroscopy. *Journal of the American Chemical Society* **114,** 6182–6189 (1992).

49. Hunger, M., Freude, D., Fröhlich, T., Pfeifer, H. & Schwieger, W. 1H-MAS nmr studies of ZSM-5 type zeolites. *Zeolites* **7,** 108–110 (1987).

50. Dib, E., Costa, I. M., Vayssilov, G. N., Aleksandrov, H. A. & Mintova, S. Complex H-bonded silanol network in zeolites revealed by IR and NMR spectroscopy combined with DFT calculations. *Journal of Materials Chemistry A* **9,** 27347–27352 (2021).

51. Zecchina, A., Bordiga, S., Spoto, G., Marchese, L., Petrini, G., Leofanti, G. & Padovan, M. Silicalite characterization. 2. IR spectroscopy of the interaction of carbon monoxide with internal and external hydroxyl groups. *The Journal of Physical Chemistry* **96,** 4991–4997 (1992).

52. Woolery, G., Alemany, L., Dessau, R. & Chester, A. Spectroscopic evidence for the presence of internal silanols in highly siliceous ZSM-5. *Zeolites* **6,** 14–16 (1986).

53. Hoffmann, P. & Lobo, J. A. Identification of diverse silanols on protonated ZSM-5 zeolites by means of FTIR spectroscopy. *Microporous and mesoporous materials* **106,** 122–128 (2007).

54. Villaescusa, L., Barrett, P., Kalwei, M., Koller, H. & Camblor, M. Synthesis and physicochemical characterization of an aluminosilicate zeolite with IFR topology, prepared by the fluoride route. *Chemistry of materials* **13,** 2332–2341 (2001).

55. Schroeder, C., Siozios, V., Mück-Lichtenfeld, C., Hunger, M., Hansen, M. R. & Koller, H. Hydrogen bond formation of Brønsted acid sites in zeolites. *Chemistry of Materials* **32,** 1564–1574 (2020).

56. Hadjiivanov, K. *Identification and characterization of surface hydroxyl groups by infrared spectroscopy* in *Advances in Catalysis* **57** (Elsevier, 2014), 99–318.

57. Nesterenko, N., Thibault-Starzyk, F., Montouillout, V., Yuschenko, V., Fernandez, C., Gilson, J.-P., Fajula, F. & Ivanova, I. Accessibility of the acid sites in dealuminated small-port mordenites studied by FTIR of co-adsorbed alkylpyridines and CO. *Microporous and mesoporous materials* **71,** 157–166 (2004).

58. Kunkeler, P., Downing, R. & Van Bekkum, H. *The use of bulky molecules as probes for investigating the contributions of the external and internal pore-wall activities of zeolite catalysts* in *Studies in Surface Science and Catalysis* **137** (Elsevier, 2001), 987–1001.

59. Góra-Marek, K., Tarach, K. & Choi, M. 2, 6-Di-tert-butylpyridine sorption approach to quantify the external acidity in hierarchical zeolites. *The Journal of Physical Chemistry C* **118,** 12266–12274 (2014).

60. Lakiss, L., Vicente, A., Gilson, J.-P., Valtchev, V., Mintova, S., Vimont, A., Bedard, R., Abdo, S. & Bricker, J. Probing the Brønsted Acidity of the External Surface of Faujasite-Type Zeolites. *ChemPhysChem* **21,** 1873–1881 (2020).

61. Corma, A., Fornés, V., Forni, L., Márquez, F., Martınez-Triguero, J. & Moscotti, D. 2, 6-Di-tert-butyl-pyridine as a probe molecule to measure external acidity of zeolites. *Journal of Catalysis* **179,** 451–458 (1998).

62. Fărcaşiu, D., Leu, R. & Corma, A. Evaluation of accessible acid sites on solids by 15N NMR spectroscopy with di-tert-butylpyridine as base. *The Journal of Physical Chemistry B* **106,** 928–932 (2002).

63. Zholobenko, V., Freitas, C., Jendrlin, M., Bazin, P., Travert, A. & Thibault-Starzyk, F. Probing the acid sites of zeolites with pyridine: Quantitative AGIR measurements of the molar absorption coefficients. *Journal of Catalysis* **385,** 52–60 (2020).

64. Ghojavand, S., Dib, E., Rey, J., Daouli, A., Clatworthy, E. B., Bazin, P., Ruaux, V., Badawi, M. & Mintova, S. Interplay between alkali-metal cations and silanol sites in nanosized CHA zeolite and implications for CO2 adsorption. *Communications Chemistry* **6,** 134 (2023).

65. Hadjiivanov, K. I. & Vayssilov, G. N. Characterization of oxide surfaces and zeolites by carbon monoxide as an IR probe molecule. *Advances in Catalysis* **47,** 307–511 (2002).

66. Cairon, O. & Chevreau, T. Quantitative FTIR studies of hexagonal and cubic faujasites by pyridine and CO adsorption Numbers and relative acidity of the HF and LF zeolitic hydroxy groups. *Journal of the Chemical Society, Faraday Transactions* **94,** 323–330 (1998).

67. Kustov, L., Kazanskii, V., Beran, S., Kubelkova, L. & Jiru, P. Adsorption of carbon monoxide on ZSM-5 zeolites: infrared spectroscopic study and quantum-chemical calculations. *Journal of Physical Chemistry* **91,** 5247–5251 (1987).

68. Peri, J. B. & Hannan, R. B. Surface hydroxyl groups on γ-alumina1. *The Journal of Physical Chemistry* **64,** 1526–1530 (1960).

69. Peri, J. Infrared and gravimetric study of the surface hydration of γ-alumina. *The Journal of Physical Chemistry* **69,** 211–219 (1965).

70. Gramatikov, S. P., Petkov, P. S. & Vayssilov, G. N. The relative stability of SCM-14 germanosilicate with different distributions of germanium ions in the absence and presence of structure-directing agents. *Inorganic Chemistry Frontiers* **9,** 3747–3757 (2022).

71. Dib, E., Mineva, T., Veron, E., Sarou-Kanian, V., Fayon, F. & Alonso, B. ZSM-5 zeolite: complete Al bond connectivity and implications on structure formation from solid-state

NMR and quantum chemistry calculations. *The Journal of Physical Chemistry Letters* **9,** 19–24 (2018).

72. Corma, A., Garcia, H. & Primo, J. Influence of the acid-strength distribution of the zeolite catalyst on the t-butylation of phenol. *Journal of chemical research. Synopses (Print)*, 40–41 (1988).

73. Zhang, K., Zhang, H., Xu, G., Xiang, S., Xu, D., Liu, S. & Li, H. Alkylation of phenol with tert-butyl alcohol catalyzed by large pore zeolites. *Applied Catalysis A: General* **207,** 183–190 (2001).

74. Zhang, K., Huang, C., Zhang, H., Xiang, S., Liu, S., Xu, D. & Li, H. Alkylation of phenol with tert-butyl alcohol catalysed by zeolite Hβ. *Applied Catalysis A: General* **166,** 89–95 (1998).

75. Guisnet, M. & Pinard, L. Characterization of acid-base catalysts through model reactions. *Catalysis Reviews* **60,** 337–436 (2018).

76. Lercher, J. A., Jentys, A. & Brait, A. Catalytic test reactions for probing the acidity and basicity of zeolites. *Acidity and Basicity*, 153–212 (2008).

77. Prasomsri, T., To, A. T., Crossley, S., Alvarez, W. E. & Resasco, D. E. Catalytic conversion of anisole over HY and HZSM-5 zeolites in the presence of different hydrocarbon mixtures. *Applied Catalysis B: Environmental* **106,** 204–211 (2011).

78. Zhu, X., Mallinson, R. G. & Resasco, D. E. Role of transalkylation reactions in the conversion of anisole over HZSM-5. *Applied Catalysis A: General* **379,** 172–181 (2010).

79. Jia, L., Raad, M., Hamieh, S., Toufaily, J., Hamieh, T., Bettahar, M., Mauviel, G., Tarrighi, M., Pinard, L. & Dufour, A. Catalytic fast pyrolysis of biomass: superior selectivity of hierarchical zeolites to aromatics. *Green Chemistry* **19,** 5442–5459 (2017).